Review of experimental and analytical techniques to determine H, C, N, and S solubility and metal–silicate partitioning during planetary differentiation

Celia Dalou, Terry-Ann Suer, Laurent Tissandier, Weronika L Ofierska, Alice Girani, Paolo A Sossi

▶ **To cite this version:**

Celia Dalou, Terry-Ann Suer, Laurent Tissandier, Weronika L Ofierska, Alice Girani, et al.. Review of experimental and analytical techniques to determine H, C, N, and S solubility and metal–silicate partitioning during planetary differentiation. Progress in Earth and Planetary Science, 2024, 11, pp.27. ⟨10.1186/s40645-024-00629-8⟩. ⟨hal-04680730⟩

HAL Id: hal-04680730

https://hal.science/hal-04680730v1

Submitted on 29 Aug 2024

HAL is a multi-disciplinary open access archive for the deposit and dissemination of scientific research documents, whether they are published or not. The documents may come from teaching and research institutions in France or abroad, or from public or private research centers.

L'archive ouverte pluridisciplinaire **HAL**, est destinée au dépôt et à la diffusion de documents scientifiques de niveau recherche, publiés ou non, émanant des établissements d'enseignement et de recherche français ou étrangers, des laboratoires publics ou privés.

HAL Authorization

Dalou *et al.*
Progress in Earth and Planetary Science (2024) 11:27
https://doi.org/10.1186/s40645-024-00629-8

Progress in Earth and Planetary Science

REVIEW

Open Access

Review of experimental and analytical techniques to determine H, C, N, and S solubility and metal–silicate partitioning during planetary differentiation

Celia Dalou[1*], Terry-Ann Suer[2], Laurent Tissandier[1], Weronika L. Ofierska[3], Alice Girani[3] and Paolo A. Sossi[3]

Abstract

During their formation, terrestrial planets underwent a magma ocean phase during which their metallic cores segregated from their silicate mantles and their early atmospheres formed. These planetary formation processes resulted in a redistribution of the abundances of highly volatile elements (HVEs, such as H, C, N, and S) between the planets' metallic cores, silicate mantles, and atmospheres. This review presents the numerous experimental techniques used to simulate the conditions and identify the parameters that influenced the behavior of HVEs during planetary formation. We also review the analytical techniques used to characterize the different types of experimental samples and quantify the distribution of HVEs between metallic and silicate phases, as well as their solubilities in silicate glasses. This exhaustive review targets students and young researchers beginning their work on the subject, or, more generally, scientists seeking a better understanding of this field of research.

Keywords Differentiation, Magma ocean, Core formation, Evaporation, Experimental techniques, Low-pressure, High-pressure, Oxygen fugacity, Analytical techniques, Partition coefficients

1 Introduction

The development of life-supporting molecules depends on the availability of volatile elements (H, C, N, O, S) at a planet's surface, which, alongside other critical parameters, has allowed the development and maintenance of a stable biosphere on Earth (Kasting and Siefert 2002). The prevailing surface conditions on terrestrial planets were mainly determined by the composition of their atmospheres and the existence (or lack) of a magnetic field protecting their surfaces from solar winds. Furthermore, the long-term stability of these surface conditions hinges upon the prevalence and rates of plate tectonics, which recycles volatile elements between a planet's interior and its surface (e.g., Dehant et al. 2007; Foley and Driscoll 2016). However, these present-day conditions are not representative of the entire history of a rocky planet, which, at times, was partially to completely molten, i.e., characterized by a magma ocean stage(s). Magma oceans are thought to have facilitated metallic core segregation, as well as the formation of early atmospheres, via solidification and degassing. Thus, the magma ocean stage likely set the initial volatile element distributions between the interiors and surfaces of rocky planets (Elkins-Tanton 2008).

The current composition of a terrestrial planet's core depends not only on the bulk composition of the planet, but also on the solubility of volatile elements in the magma ocean and the metal–silicate partition

*Correspondence:
Celia Dalou
celia.dalou@univ-lorraine.fr
[1] Université de Lorraine, CNRS, CRPG, 54000 Nancy, France
[2] Laboratory for Laser Energetics, University of Rochester, Rochester, NY, USA
[3] Institute of Geochemistry and Petrology, ETH Zürich, 8092 Zurich, Switzerland

Springer Open

© The Author(s) 2024. **Open Access** This article is licensed under a Creative Commons Attribution 4.0 International License, which permits use, sharing, adaptation, distribution and reproduction in any medium or format, as long as you give appropriate credit to the original author(s) and the source, provide a link to the Creative Commons licence, and indicate if changes were made. The images or other third party material in this article are included in the article's Creative Commons licence, unless indicated otherwise in a credit line to the material. If material is not included in the article's Creative Commons licence and your intended use is not permitted by statutory regulation or exceeds the permitted use, you will need to obtain permission directly from the copyright holder. To view a copy of this licence, visit http://creativecommons.org/licenses/by/4.0/.

coefficients of H, C, N, O, and S, which vary with pressure, temperature, and oxygen fugacity. Over the last two decades, the effects of these conditions on the redistribution of highly volatile elements (HVEs; here, H, C, N, and S) have been investigated experimentally by simulating magma ocean degassing and core formation on different rocky planets. Such experiments are used to determine HVE solubilities and metal–silicate partition coefficients, respectively.

Large-volume apparatuses have been used in most of these experimental studies, achieving pressures from 0.5 to 24 GPa and temperatures up to 2400 °C (e.g., Roskosz et al. 2013; Boujibar et al. 2014; Chi et al. 2014; Li et al. 2016; Dalou et al. 2017; Clesi et al. 2018; Malavergne et al. 2019; Grewal et al. 2019, 2021; Fichtner et al. 2021). Recently, superliquidus (i.e., melting) experiments performed in laser-heated diamond anvil cells (LHDACs) have extended the range of these measurements to conditions considered relevant to core formation on Earth (i.e., ≥ 45–55 GPa, ≥ 4000 °C; e.g., Suer et al. 2017; Mahan et al. 2018; Fischer et al. 2020; Tagawa et al. 2021; Blanchard et al. 2022). HVE solubility measurements in silicate liquids complement these metal–silicate partitioning measurements and have enhanced our knowledge of volatile outgassing and cycling between Earth's early mantle and atmosphere (e.g., Libourel et al. 2003; Hirschmann et al. 2012; Ardia et al. 2013; Armstrong et al. 2015; Newcombe et al. 2017; Boulliung et al. 2020; Bernadou et al. 2021; Dalou et al. 2022; Sossi et al. 2023). The choice of analytical techniques (bulk or local mass spectrometry, nuclear microprobe, or vibrational spectroscopy) to characterize HVE concentrations in both metal and silicate phases depends on several criteria, including the sizes and textures of experimental samples and anticipated HVE concentrations in different phases.

Oxygen comprises ~ 44 wt.% of Earth's mantle and, by extension, a similar fraction of the silicate mantles of other terrestrial planets; it therefore plays a key role in determining the speciation of volatile elements in atmospheres and mantles or magma oceans. The abundance of O relative to the other rock-forming elements, together with the pressure–temperature conditions at the surface of a magma ocean, determines the oxygen fugacity (fO_2) at the surface. Because O is far in excess of the other major atmosphere-forming elements (the HVEs) in magma oceans, the fO_2 dictates their relative fugacities (e.g., the CO/CO_2 and H_2/H_2O ratios) in the atmosphere (Hirschmann 2012; Sossi et al. 2020a). Moreover, because different gaseous molecules have different solubilities in silicate liquids (e.g., Yoshioka et al. 2019; Bower et al. 2022), the HVE distributions between planetary interiors and atmospheres depend on fO_2. On Earth, iron is by far the most abundant redox-sensitive element, and, because the oxygen abundance in geologically relevant phases is rarely measured directly (if ever), the redox state of iron (Fe^{3+}/Fe^{2+}) is a key proxy for the fO_2 of a system, be it rock, fluid, or gas.

In this review, we summarize the above-mentioned experimental and analytical techniques, as well as the limitations and challenges associated with each experimental technique and chemical analyses of experimental charges.

2 Defining partitioning and solubility

2.1 Partitioning

In terrestrial planets, core formation represents the largest mass transfer event in their history. The partitioning of elements between silicate and metallic phases can be generally described as:

$$E^{n+}O_{\frac{n}{2}\,\text{silicate melt}}^{n-} = E^{0}_{\text{molten metal}} + \frac{n}{4}O_{2_{\text{gas}}}, \quad (1)$$

where n is the oxidation state of element E dissolved in the silicate melt. By definition, in its metallic form, element E has zero net charge. Hence, at equilibrium:

$$K = \frac{a\left(E^{0}\right)\cdot f(O_2)^{n/4}}{a\left(E^{n+}O_{\frac{n}{2}}^{n-}\right)} = D_i^{\text{metal-silicate}}\cdot\frac{\gamma\left(E^{0}\right)\cdot f(O_2)^{n/4}}{\gamma\left(E^{n+}O_{\frac{n}{2}}^{n-}\right)}, \quad (2)$$

where K is the equilibrium constant, a the activity, γ the activity coefficient, and f the fugacity. The partition coefficient of an element of interest i between metallic and silicate phases, $D_i^{\text{metal-silicate}}$, is defined as $X_i^{\text{metal}}/X_i^{\text{silicate}}$, where X denotes the mole fraction concentration of that element in each phase. Hence, the quantity $D_i^{\text{metal-silicate}}$ in Eq. 2 is proportional to the molar ratio of element i in the silicate and metallic phases. Were core formation to have occurred at equilibrium (or incomplete equilibrium; Zube et al. 2019), elements would have distributed between the Fe-rich metallic phase and the silicate mantle according to their thermodynamically governed partition coefficients. Consequently, elements with high $D_i^{\text{metal-silicate}}$ values are siderophile and strongly depleted in the mantle, whereas those with low $D_i^{\text{metal-silicate}}$ values are lithophile and should theoretically remain in chondritic proportions in the mantle (Wade and Wood 2005).

The equilibrium constant, K, is related to the Gibbs Free Energy change of the reaction (ΔG_{rxn}) through:

$$\Delta G_{\text{rxn}} = -RT\ln K. \quad (3)$$

Because both phases involved in the reaction are liquids, to a first order, the entropy terms of the free

energy reaction are likely to be small, and partitioning can be approximated as:

$$\ln D_i^{\text{metal-silicate}} \approx \Delta H/RT, \tag{4}$$

where ΔH is related to the enthalpy of the reaction terms. Importantly, because ΔH is nearly independent of temperature, the partition coefficient D tends to unity at infinite temperature.

Pressure changes are more difficult to predict, as they depend upon the partial molar volumes and compressibilities of the volatile species in both the silicate liquid and the metal. This is governed by:

$$\left(\frac{d\ln D_i^{\text{metal-silicate}}}{dP}\right)_T = \frac{\Delta V^0}{RT}, \tag{5}$$

which, when integrated, gives:

$$\ln\left(\frac{D_{i,1}^{\text{metal-silicate}}}{D_{i,2}^{\text{metal-silicate}}}\right)_T = -\frac{\Delta V^0}{R}(P_2 - P_1), \tag{6}$$

where ΔV^0 is the molar volume change in the mass action equation, showing that $\ln D_i^{\text{metal-silicate}}$ is proportional to P (e.g., by taking P_1 as 1 bar). Under the conditions of core formation, HVEs are expected to be at least partially dissolved in the magma ocean (see Sect. 2.2, below), and the system does not contain a gas phase; in this case, it is seldom important to consider the pressure dependence. The volume change of the reaction, even if ΔV^0 is constant, only plays a significant role when the pressure integral is large enough (e.g., the pressure range relevant to core formation).

Alternatively, metal–silicate partitioning can be expressed using the exchange coefficient with Fe (the dominant component of planetary cores), K_D, such as:

$$EO_{\frac{n}{2}} + \frac{n}{2}\text{Fe} \Leftrightarrow \frac{n}{2}\text{FeO} + E, \tag{7}$$

$$\text{and, } K_D = D_i^{\text{metal-silicate}}/D_{\text{Fe}}^{n/2}. \tag{8}$$

where K_D is related to the equilibrium constant K of reaction (2), which can be defined in terms of K_D and the activity coefficients (γ) of the metal and silicate phases by combining with Eq. 2 as:

$$\ln K = \ln K_D + \ln\frac{\gamma_E^{\text{metal}}}{\left(\gamma_{\text{Fe}}^{\text{metal}}\right)^{n/2}} + \ln\frac{\left(\gamma_{\text{FeO}}^{\text{silicate}}\right)^{n/2}}{\left(\gamma_{EO_{n/2}}^{\text{silicate}}\right)} = a + \frac{b}{T} + c\frac{P}{T}. \tag{9}$$

Then, $\ln D_i^{\text{metal-silicate}}$ can also be expressed in terms of the above variables and constants as:

$$\ln D_i^{\text{metal-silicate}} = a + \frac{b}{T} + c\frac{P}{T} - d\frac{\text{IW}}{2} - \ln\frac{\gamma_E^{\text{metal}}}{\left(\gamma_{\text{Fe}}^{\text{metal}}\right)^{n/2}}, \tag{10}$$

where IW is the iron–wüstite redox buffer:

$$\text{IW} = -2\log_{10}\frac{a_{\text{Fe}}}{a_{\text{FeO}}} = -2\log_{10}\frac{\gamma_{\text{Fe}}X_{\text{Fe}}}{\gamma_{\text{FeO}}X_{\text{FeO}}}. \tag{11}$$

The constants *a, b, c,* and *d* are determined using multivariate least-squares linear regression of the measured $D_i^{\text{metal-silicate}}$, P, T, and phase compositions (e.g., Wade and Wood 2005; Chidester et al. 2022; Suer et al. 2023). In other words, Eq. (10) allows us to constrain the dependence of the partition coefficients on P, T, and fO_2.

2.2 Solubility

The solubility of a given species describes its capacity to dissolve into a condensed phase. Determining the solubilities of major atmosphere-forming elements in silicate liquids is therefore central to understanding the composition of the primitive atmosphere. The most abundant molecule in Earth's atmosphere, N_2, dissolves in silicate liquids at high oxygen fugacities as (Libourel et al. 2003):

$$N_{2\text{gas}} = N_{2\text{liquid}}, \tag{12}$$

implying an equilibrium relationship of the kind:

$$K = a(N_2)/f(N_2). \tag{13}$$

Therefore, solubility laws require that the fugacity of the relevant gaseous species and the mole fraction of the dissolved species in the melt be defined. In such scenarios, and if the quantity of the dissolved species is sufficiently dilute so as not to perturb the structure of the solvent (silicate liquid), the solubilities can be fit to Henry's Law as:

$$X(N_2) = \alpha f(N_2)^{\beta}. \tag{14}$$

where X is the mole fraction, α is proportional to the quotient of K and the activity coefficient of N_2, and β is the stoichiometric coefficient. Some species show departures from Henry's Law: notably, the dissolution reaction of H_2O defines $\beta = 0.5$ at low fH_2O (Hamilton et al. 1964; Newcombe et al. 2017; Sossi et al. 2023). Therefore, controlling fugacity in experiments is invaluable for defining solubility laws. Moreover, the equilibrium constant K (and hence α) changes with temperature owing to the free energy change of the reaction, which can be determined by varying T while keeping other variables constant.

Many homogeneous gas-phase reactions between major atmosphere-forming species are, in turn, dependent on fO_2. For example:

$$H_{2gas} + \frac{1}{2}O_{2gas} = H_2O_{gas}, \quad (15)$$

$$CO_{gas} + \frac{1}{2}O_{2gas} = \frac{1}{2}CO_{2gas}, \quad (16)$$

$$CO_{gas} + H_{2gas} + \frac{1}{2}O_{2gas} = CH_{4gas} + 2OH_{gas}. \quad (17)$$

Consequently, varying fO_2 at constant P and T in the C–O system will control the CO/CO_2 ratio of the gas phase. Hence, a change of the Henrian solubility constants upon a change in fO_2 may indicate a change in gas-phase speciation.

3 Experimental techniques

The diversity of conditions to be tested to simulate different planetary environments implies the use of a wide range of experimental setups. They mainly differ in terms of the P–T conditions they can attain. Each high-pressure technique can be used to assess the unique thermodynamic states of planet-forming materials at P–T ranges relevant to core–mantle differentiation in bodies of sizes ranging from asteroids to large terrestrial planets. In contrast, 1-atm devices used for solubility experiments differ mainly in terms of sample mass, quench speed, and fO_2 control. Compositional analyses of these samples are typically performed ex situ, and solubility data and partition coefficients are determined by the concentration ratios of elements of interest between the metal and silicate phases. Among the parameters to be evaluated before experimentation, the size of the sample is critical because it constrains the type of analyses that can be performed.

3.1 Large-volume apparatuses

3.1.1 Low-pressure devices for solubility experiments

In contrast to high-pressure experiments, low-pressure studies can be performed under open-system conditions (that is, mass can be lost from the experimental charge) at (near-)ambient pressures, as is the case for levitation and vertical-furnace experiments. Both techniques are performed in large reacting chambers (from tens of cubic centimeters to several liters), meaning that evaporated species are able to leave the immediate vicinity of the heated sample (e.g., Donaldson 1979). Furthermore, fO_2 (and the fugacities of other gaseous species) can be set by continuously flowing gas mixtures, the nature of which depend on the conditions to be tested. This is the key advantage of low-pressure conditions: because high-temperature vapors behave essentially ideally at 1 bar, their thermodynamic quantities are precisely known (e.g., from the JANAF tables; Chase 1998) and their fugacities for a given bulk gas composition are easily defined (to within a few percent relative). Because HVEs have stable gas species at standard temperature and pressure (STP), such as N_2, CO_2, CO, H_2, SO_2, and O_2, the gas flow rates can be precisely controlled to accurately fix fN_2, fCO_2, fCO, and so on.

In contrast, sealed silica tubes are closed systems, and metallic buffers or reducing/oxidizing species must be added within the tube to control the fO_2.

3.1.1.1 Aerodynamic levitation furnaces This kind of furnace is mainly composed of a conical nozzle, with a central hole from which a gas or gas mixture flows. The gas flows at typical velocities of the order of ~ 10 m/s (hundreds of cubic centimeters per minute, depending on the nozzle diameter) and is used to stably levitate the sample (e.g., Nordine and Atkins 1982; Pack et al. 2010). Additionally, the gas can also be used to control the fO_2, or indeed the fugacity of the desired gaseous species, since the gas compositions can be changed by mixing H_2, CO_2, and Ar gases using multiple gas flow controllers (Badro et al. 2021).

In most of these devices, the sample is heated by a ~ 100 W continuous-wave CO_2 laser with a wavelength of 10.6 µm that is focused to a spot diameter of 1–5 mm depending on the size of the sample (Fig. 1). Other heating sources (solar furnaces, mirror furnaces) have also been used for specific applications, but are more difficult to implement (Oran and Berge 1982). Temperatures can be very high (e.g., > 3000 °C using laser heating), but can easily be adapted according to the process of interest (see reviews by Hennet et al. 2006 and Pack et al. 2010).

The main benefit of this technique is the absence of contact with the sample container during the experiment, preventing chemical interactions with the container (e.g., Fe is not lost into Pt wires or crucibles, and samples are not contaminated with Al_2O_3 or its impurities, as in vertical tube furnaces). Moreover, crystallization is unaffected by heterogeneous nucleation along the container surface. Other advantages include (1) the possibility of reaching very high temperatures (> 3000 °C) and (2) very short experimental durations owing to the low sample mass, which allows rapid heating/cooling cycles and results in quench rates of ~ 850 °C/s for ~ 2-mm-diameter spheres (Badro et al. 2021). These specificities have been exploited to make peridotitic glasses as analogs of magma oceans (e.g., Sossi et al. 2020b). Otherwise, homogeneous peridotitic samples have been prepared by a sol–gel process, which often contains a moderate amount of water (Auzende et al. 2011).

However, the small volume of the heated sample complicates temperature measurements, accomplished using an optical pyrometer rather than thermocouples. Although such pyrometers have precision on the

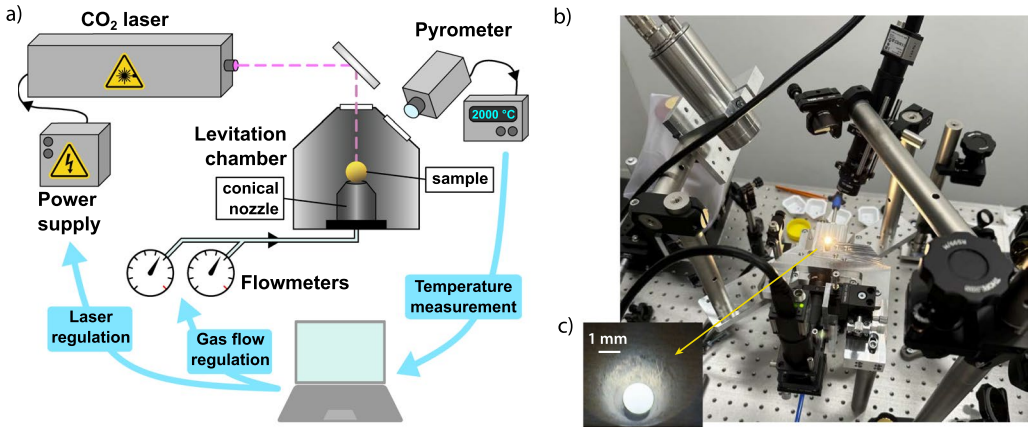

Fig. 1 Aerodynamic levitation furnace. **a** Schematic of the setup modified from Ni et al. (2021). **b** Photograph of the setup at the Eidgenössische Technische Hochschule (ETH, Zürich, Switzerland), and **c** zoom of the levitated sphere (modified from Badro et al. 2021)

order of a few degrees, instability in the laser heating can result in fluctuations of ~ 50 °C (Sossi et al. 2023). Moreover, the unknown emissivities of some liquids at the wavelength(s) of the pyrometer means that additional calibration is required to derive absolute temperatures (e.g., Sarou-Kanian et al. 2005; Taguchi et al. 2023). Depending on the geometry of the furnace (especially for single-laser devices), the combination of laser heating and the cooler gas stream on the sample may induce a thermal gradient despite the rotation of the sample during the run (as observed in Hennet et al. 2006). To remedy this, dual laser setups are common, and a third laser can even be added to offset cooling induced by the gas (Hennet et al. 2006). The relatively high gas flow rates required to stably levitate a sample (several hundreds of standard cubic centimeters per minute; Landron et al. 2000; Pack et al. 2010) promote mixing and hence a constant fO_2. However, such high flow rates increase the advection of evaporated species from the surface (see Charnoz et al. 2021 and Young et al. 2022 for theoretical treatments), promoting further evaporation. Because the system is open to mass transport and the sample has a finite mass, this evaporation (unless congruent) changes the composition of the residual sample. Indeed, this environment can result in the evaporation of volatile and moderately volatile elements (mainly the alkalis, S, F, and Cl, but also Mn, Cr, and Zn; Sossi et al. 2019), which are then carried away from, and thus depleted in, the sample (Pack et al. 2010; Badro et al. 2021; Ni et al. 2021).

Consequently, levitation furnaces are best suited to the study of high-temperature materials or those with low volatile abundances, although they can also be gainfully used to investigate thermodynamically unequilibrated processes such as evaporation.

3.1.1.2 Vertical drop-quench furnaces This furnace design has long been employed in petrological studies to examine phase relations, evaporation, crystallization, textural relationships, and partition coefficients between phases. High temperatures up to ~ 1700 °C are reached at 1 atm using metallic heating elements (usually $MoSi_2$, but graphite is also feasible). Experiments are performed within a refractory tube (mainly Al_2O_3, but sometimes SiO_2 or SiC for lower or higher T experiments, respectively) in which gas mixtures can be pumped to control the fugacities of oxygen and other elements. Samples are held in the hot zone of the furnace (typically ~ 3 cm long) by metallic wires (often Pt, but also Ir, W, and Re for more reduced atmospheres) or metallic/refractory crucibles (such as Pt or Al_2O_3) and are efficiently quenched (> 700 °C/s, as estimated from the decrease in sample brightness within ~ 1 s) by dropping them into the lower, cold part of the furnace, sometimes directly into a water bath (Fig. 2).

The main advantage of vertical drop-quench furnaces is that the experimental temperature is precisely and accurately controlled. Absolute temperatures are calibrated using metals whose melting points are known to within ~ 1–2 °C (usually Au at 1064 °C and Pd at 1555 °C). Moreover, these furnaces can often be programmed to follow complex thermal histories, which is more relevant to natural samples than simple isothermal experiments. Another benefit is the possibility of varying the sample size: small samples (~ 10 mg) can be useful to quickly reach equilibrium with the gas phases (i.e., in a few minutes), and different surface/volume ratios can be tested, for example, to obtain information about evaporation processes (e.g., Mathieu et al. 2008). Gas flow rates may also be precisely controlled, varied over a relatively wide

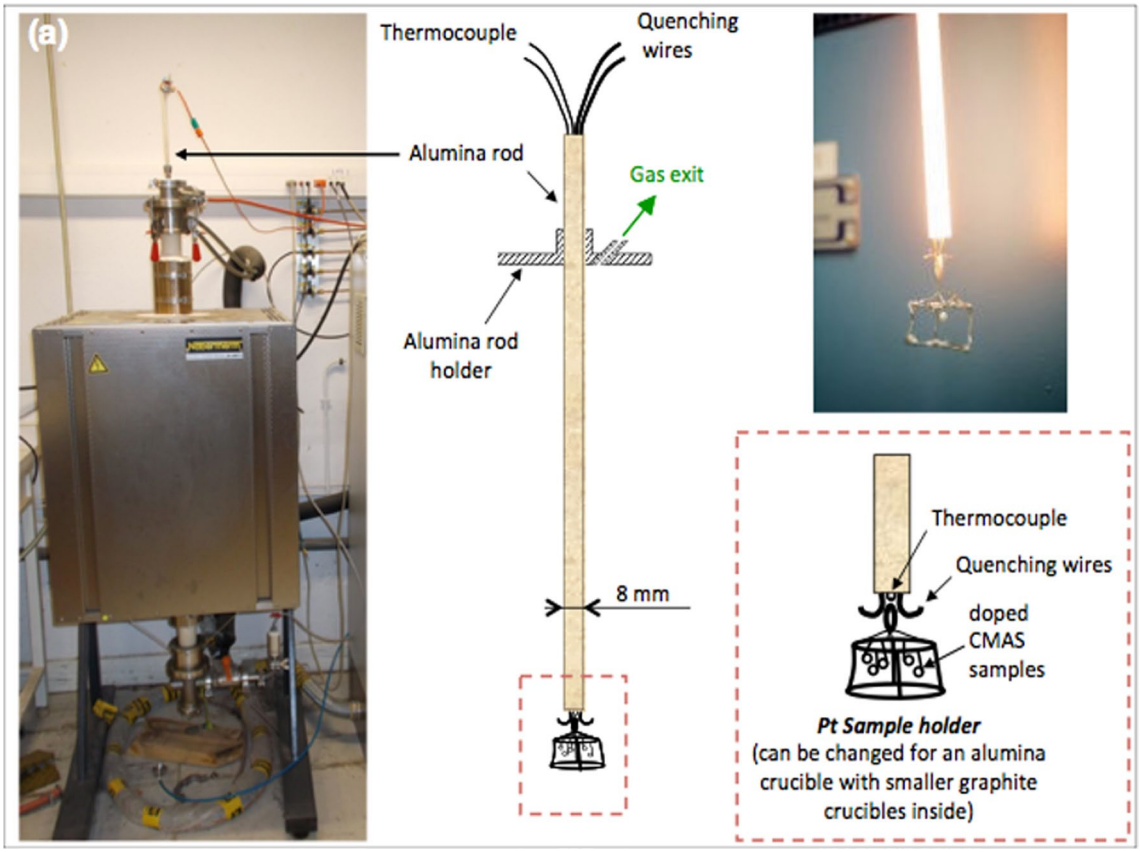

Fig. 2 Photographs and a schematic of the vertical drop-quench furnace at the Centre de Recherches Pétrographiques et Géochimiques (CRPG, Nancy, France)

range (typically tens to hundreds of standard cubic centimeters per minute), or varied systematically with time to simulate changing fugacity conditions (e.g., Prabha-Mohan et al. 2023). Oxygen fugacities are typically independently measured by means of the electromotive force (emf) via an oxygen probe ($SIRO_2$; Badwal et al. 1987; Mendybaev et al. 1998) composed of an yttria-stabilized zirconia (YSZ) solid electrolyte and Pt electrode.

One of the limitations of 1-atm furnaces is the necessity of using sample containers. Generally, samples should not contain elements that readily alloy with the sample container at the conditions of the experiment; for example, the use of Pt in the well-known wire-loop method (Presnall and Brenner 1974; Donaldson et al. 1975) is problematic if the silicate melt contains iron. Indeed, if the mass of the container is large enough, alloying can modify the composition of the sample and the thermal resistance of the wire (Presnall and Brenner 1974; Corrigan and Gibb 1979). One approach to overcome this issue is to use a pre-alloyed container, although this adds to the experimental preparation time (Grove 1982).

Another limitation, as with other open-system devices, is the evolution of the sample composition due to evaporation of the most volatile species (e.g., O'Neill 2005; Sossi et al. 2019), although this process is slower than in a levitation furnace due to the lack of advection. If undesired, this effect can be mitigated by adding the volatiles of interest to the atmosphere in the furnace (Amalberti et al. 2018; Boulliung et al. 2020; Boulliung and Wood 2022) or by adding a supplementary volatile source, such as a bucket containing the volatile compound of interest (e.g., Georges et al. 2000; O'Neill 2005; Borisov 2008). However, experiments using a supplementary volatile source are difficult to undertake and typically only reach a steady state rather than true equilibrium.

In summary, vertical furnaces are very thermally stable and thus suitable for solubility and evaporation experiments. However, they are prone to evolving sample compositions that may preclude their use for naturally relevant studies.

3.1.1.3 Sealed silica tubes Sealed silica tubes are intermediate between the open-system protocols previously

described and the closed-system high-pressure devices described in the next subsections. These devices are closed systems that are run at low pressures (~0.1 to a few bars for experiments at temperatures relevant to magmatic systems). They contain the sample(s) and, if needed, a metallic buffer (Fig. 3a) or a graphite crucible (Fig. 3b) to control fO_2 and a 'source' of the element to be tested (Fig. 3). The tubes are prepared at room temperature and must be evacuated (to ~ 10^{-2} mbar) before sealing to accommodate the overpressure upon heating. Once closed, the tubes are inserted into a furnace (usually muffle furnaces, sometimes vertical furnaces).

The sizes (diameter and length) of the tubes can be adapted to a given study depending on the materials necessary, potentially varying the tube volume from ~ 1 to ~ 100 cm^3. Other factors controlling tube size are the ease of shaping the tubes (it becomes difficult to seal small bulbs with a torch) and the size of the furnace chamber.

In contrast to open-system devices, sample compositions will be only moderately affected by evaporation in sealed tubes; indeed, the most volatile elements will start to volatilize, but will eventually reach their vapor saturation pressure, preventing further loss from the sample

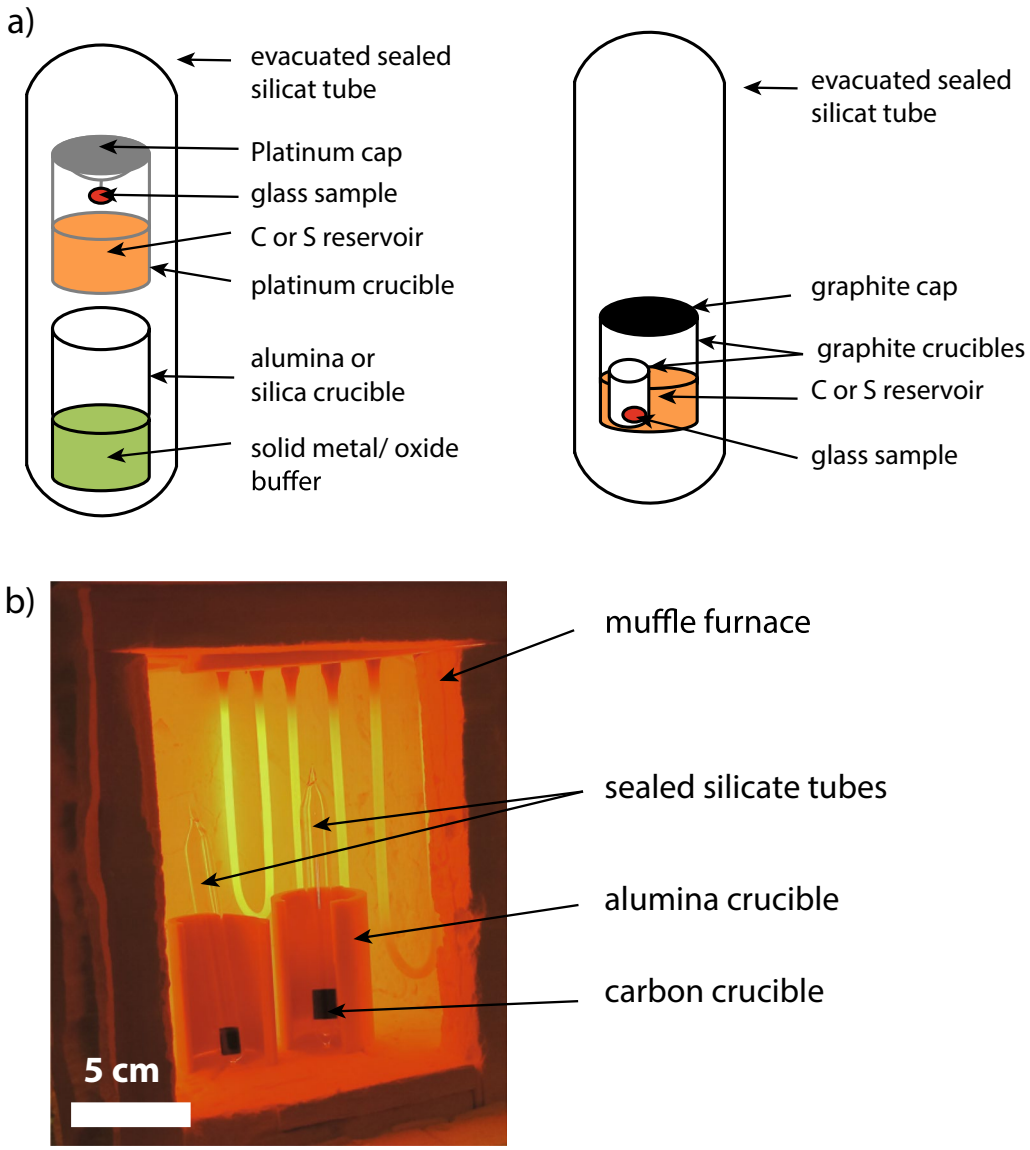

Fig. 3 **a** Schematics of two different sealed silica tube experimental designs (modified from Chevreux et al. 2021). **b** Photograph of two sealed silica tube experiments in a muffle furnace, standing in alumina crucibles (courtesy of Mahaud Chavanieu, CRPG)

(Khedim et al. 2008; Chevreux et al. 2021; Cartier et al. 2023). That said, a volatile source can be added to the tube to, at high temperature, produce a gas that will interact with the sample, allowing the "ingassing" of various elements (Mathieu et al. 2008, 2011). The closed-system nature of these experiments also constrains the conditions that can be tested. First, the fO_2 must be imposed by metallic buffers or by adding oxidizing or reducing elements to the samples, making it difficult to test a large fO_2 range. Moreover, the use of metallic buffers can preclude some applications; for example, in S solubility experiments, S reacts with metallic buffers to produce sulfides.

Due to the pressure differential between the inside and the outside of the tube (i.e., the atmosphere), the tubes can deform or even be punctured in high-temperature runs. Consequently, temperatures as high as 1450 °C are difficult to test, even in short runs of a few hours, and temperatures should not exceed 1400 °C for longer runs (> 24 h). Thus, sealed silica tubes are a good protocol for performing solubility and controlled evaporation experiments for volatile or moderately volatile elements (S, alkalis, etc.) because they can last from a few minutes to several days. Although experimental limitations (temperature, testable elements, etc.) can limit their applications, sealed silica tubes are a good compromise for low-pressure, closed-system experiments.

3.1.2 Large-volume moderate- to high-pressure devices (LVP)

Internally heated pressure vessels (IHPVs) are designed for experimental studies at medium to high temperatures (up to 1400 °C) and pressures up to 1 GPa, whereas piston-cylinder apparatuses can reach temperatures up to 2000 °C and pressures of 0.5–4 GPa (or, rarely, 6 GPa). These two apparatuses are therefore limited to experiments investigating the first hundreds of kilometers of terrestrial magma oceans, but are appropriate for studying core–mantle equilibration on smaller planetary bodies like the Moon or Mercury (≤ 5 GPa; Rai and van Westrenen 2014; Cartier and Wood 2019). In contrast, multi-anvil presses are used to attain pressures of 5–25 GPa and temperatures up to 3000 °C, conditions more relevant to core–mantle segregation on larger planets (Bouhifd and Jephcoat 2011; Rai and van Westrenen 2013).

3.1.2.1 Internally heated pressure vessels (IHPVs) IHPVs consist of a thick-walled metallic pressure vessel sealed by closure plugs at both ends, in which the pressure is applied by a gas. The pressure medium is injected in gaseous form using two multipliers and piston systems capable of reaching pressures up to 1 GPa. The injected gas is most often Ar, but can also be a mix of Ar and H in variable proportions, making it possible to simulate more reducing environments. The sample is heated by an internal-resistance two-loop tube furnace heater (Mo wiring, 17 mm internal diameter), which can reach temperatures up to 1400 °C. The vessel is cooled using a coil in which water circulates. A plug and shutter system guarantees the watertightness of the internal part under pressure, which contains the furnace and the sample. The quenching system comprises two Pt rods which allow the sample(s) to be held in the hot part of the autoclave (Fig. 4). The sample hangs from an alumina nacelle using a fine (0.2 mm)

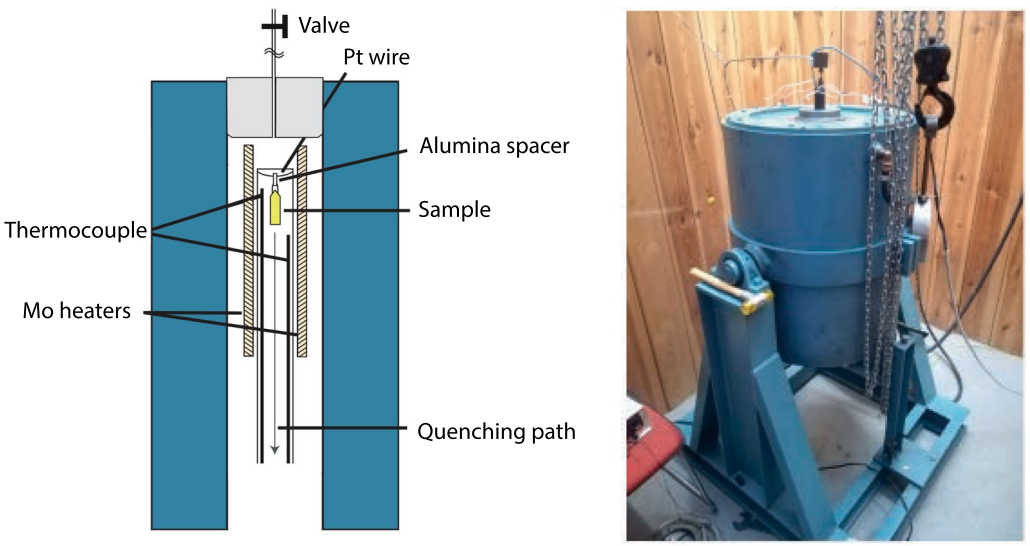

Fig. 4 Schematic diagram of an internally heated pressure vessel with rapid quench device (left) and a rapid quench IHPV at Bayerisches Geoinstitute (right, modified from Yoshioka 2018)

wire (Pt or PtRh). Quenching is performed by sending an electrical discharge into the rods to explosively fuse the wire, allowing the nacelle and the capsule(s) to fall from the hot zone of the furnace (+1000 °C) to the cold zone (−100 °C), achieving quench rates of about 500 °C/s (Holloway et al. 1992). Two to three thermocouples (e.g., S type; $Pt_{90}Rh_{10}$–Pt]) can be used at different heights in the hot zone to monitor temperature (Fig. 4); temperature gradients can vary from 0 to 20 °C over 1 cm within the hot zone.

Because Ar gas is used as the main pressure medium, pressure is known more accurately in IHPV experiments than in other large-volume apparatuses, hence the common use of IHPVs to study volatile element behaviors during magma ocean degassing (Yoshioka et al. 2019; Bernadou et al. 2021). Moreover, by adding various proportions of hydrogen to the Ar pressure medium, the oxygen fugacity can be controlled following the reaction: $H_2 + 1/2\ O_2 = H_2O$ (Gaillard et al. 2003).

3.1.2.2 Piston-cylinder apparatuses Both piston-cylinder and multi-anvil apparatuses are based on hydraulic pressure systems that drive one or two vertical hydraulic rams to compress a cylindrical cavity. Relatively large sample sizes are employed in the piston cylinder apparatus (~200 mm^3 in a 1/2″ assembly) compared to the multi-anvil type LVP. The piston-cylinder apparatus consists of a "bomb" with a centered cylindrical hole either 3/4″ (≤1.2 GPa) or 1/2″ (≥1 GPa) in diameter. The pressure on the sample chamber within the cavity is generated by pushing a piston into the cylindrical cavity. Whereas the bomb is made of pre-stressed steel rings, both the piston(s) and the core of the bomb are made of tungsten carbide (Fig. 5a). The lower ram transfers the pressure to the sample through the piston, while the upper hydraulic ram provides the end-load pressure during an experiment to support the pressure vessel from the opposite side of the master ram (Fig. 5a). In general, pressure is applied and maintained using two hand-pumps, but recently, pressure controller systems have allowed programmed pressure profiles to be executed using automatic pumps. A fraction of the hydraulic pressure is not transmitted to the sample, as evidenced by the heterogeneous pressure distribution and frictional strain between the carbide core

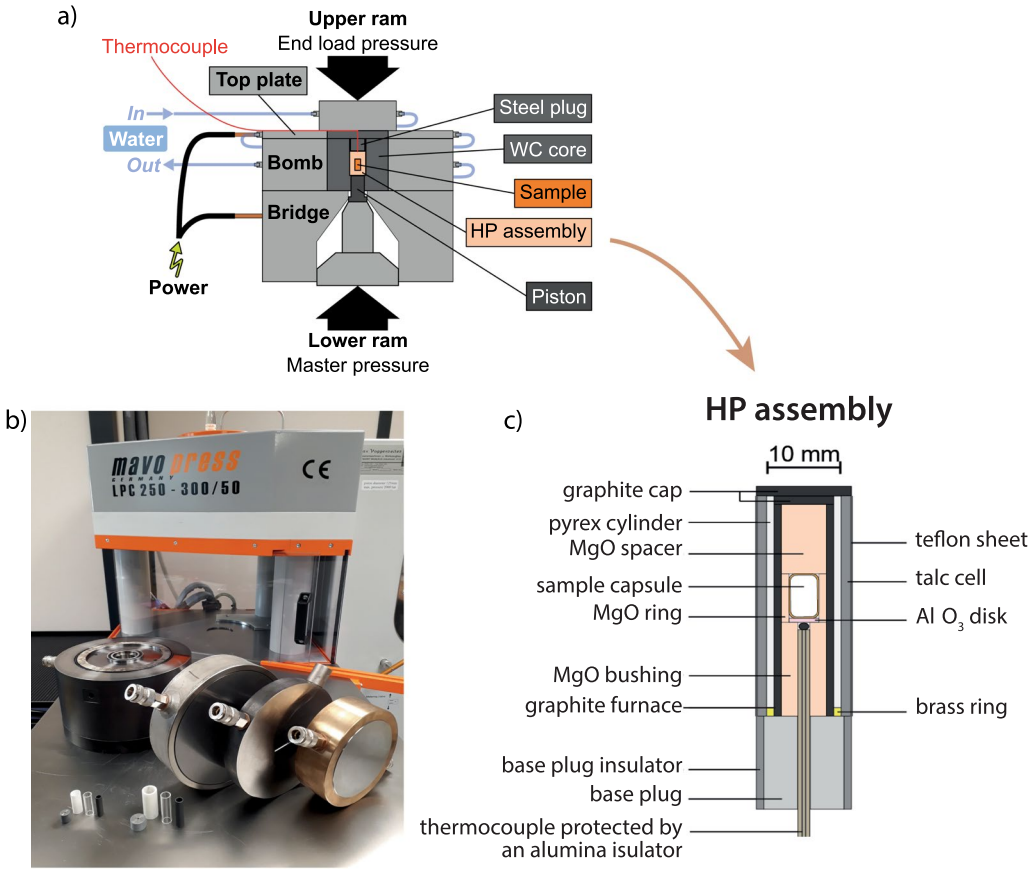

Fig. 5 **a** Schematic of the end-loaded piston-cylinder apparatus. **b** Photograph of the bridge, the bomb, the top plates and the assemblies, and **c** schematic of a 1/2″ assembly (modified from Condamine et al. 2022)

and the cell assembly, which cause pressure losses (e.g., Condamine et al. 2022) that vary with experimental pressure, temperature, and duration. Therefore, depending on the conditions of interest, a variety of piston-cylinder cell assemblies are available to transform the uniaxial pressure into hydrostatic isotropic pressure. At high temperatures (> 1600 °C), talc (Fig. 5b) or $BaCO_3$ cells should be favored over NaCl salt cells as the electrical insulator, although talc produces too much frictional strain on the carbide core and must be avoided in experiments at very high pressures (> 3 GPa, < 1600 °C; Condamine et al. 2022). Hence, special attention is required in the choice of materials used. Capsules are contained in a MgO ring sleeve sandwiched between top and bottom MgO plugs (Fig. 5c). The alumina sleeve is placed in an assemblage composed of, from innermost to outermost, graphite, pyrex, and electrical insulator cell cylinders. Finally, samples are heated electrically via copper electrodes on the top plate and the bridge, creating an electrical circuit through the resistive graphite heater (Fig. 5a). During high temperature experiments, the pressure vessel is cooled using circulating water. The electrical connection to the graphite heater is maintained through the steel plug on the top and a graphite and steel disk at the bottom of the assembly. The temperature distribution within assemblies depends on the assembly material, as described in Schilling and Wunder (2004). The experimental temperature is monitored using a thermocouple, inserted axially such that the welded junction is in close contact with the top of the capsule. Dunn and Luth (1993) reviewed the different types and best uses of thermocouples. Type-C thermocouples ($W_{95}Re_5$–$W_{74}Re_{26}$) are the most adapted to very high temperatures (up to ~ 2300 °C) for metal–silicate partitioning or magma ocean degassing experiments. At the end of the experiment, before decompression, the power to the furnace is cut and the experiment is quenched "rapidly", i.e., at ~ 130 °C/s (Ezad et al. 2023), although recent developments on new "rapid quench" piston-cylinders have improved quench rates to 160 °C/s (Ezad et al. 2023).

Both IHPVs and piston-cylinder apparatuses can be equiped with a pressure controller, allowing controlled isothermal decompression experiments. We note, however, that isothermal decompression experiments are more commonly run in the context of volcanic degassing to simulate magmas ascending through volcanic conduits (e.g., Gardner et al. 1999; Nicholis and Rutherford 2009) than to simulate the degassing of a fully molten surface in a magma ocean context.

3.1.2.3 Multi-anvil presses Multi-anvil presses are capable of generating pressures and temperatures relevant to shallow depths within Earth's lower mantle (≥ 25 GPa, 2300 °C) while maintaining a relatively large sample volume on the order of ~ 10 mm^3. Multi-anvil presses differ from piston-cylinders because the pressure is applied using a hydraulically driven ram that compresses two opposite outer guide blocks, each containing three hardened-steel primary-stage anvils that, in turn, compress eight tungsten carbide secondary anvils in multiple directions (Fig. 6a). This approach can reach 25 GPa, or even higher pressures if the anvils are made of sintered diamonds (Zhai and Ito 2011) or newer tungsten carbide anvils (TF05 and TJS01), which can reach over 30 GPa (e.g., Kunimoto et al. 2016; Ishii et al. 2017, 2022). The secondary anvils have truncated corners such that the assembly of the eight cubes into a larger single cube leaves an octahedral shaped cavity at the center (Fig. 6b), where an octahedral high-pressure ceramic cell containing the sample is placed. Samples are placed into this outer $MgO + Cr_2O_3$ octahedral ceramic pressure medium, a ZrO_2 thermal insulator, a resistance graphite or $LaCrO_3$ heater, and MgO or Al_2O_3 spacers (Fig. 6b). The addition of 5% Cr_2O_3 to the MgO pressure medium lowers its thermal conductivity. The upper component encloses a MgO tube used to accommodate the thermocouple, and a solid MgO cylindrical spacer is placed at the bottom (Fig. 6b). The middle part contains the sample capsule inside a thin MgO sleeve. In the sample area, the heater has a thicker wall to create a smaller axial thermal gradient. A molybdenum ring and disk are also used to improve electrical contact (Fig. 6b). As in the piston cylinder, current is passed through a graphite or lanthanum chromite furnace to heat the sample. For a given uniaxial load generated by the hydraulically powered guide blocks, the size of the octahedral cell assemblies (hence the truncation edge length of the WC anvils) controls the pressure generated on the sample.

As with the piston cylinder, quenching is required to "freeze" the samples to keep HVEs within the structure of high-pressure melts. For this reason, recent works have focused on improving quench rates in LVPs. Bondar et al. (2021) showed increasing the quench rate of traditional multi-anvil presses from 650 to 6700–8200 °C/s; this state-of-the-art technique currently works to pressures up to 9 GPa and temperatures up to 2200 K.

3.1.3 The critical choice of capsule materials

In general, capsules consist of welded noble metals or metallic alloys. The choice of sample capsule depends on the pressure, temperature, and oxygen fugacity of the experiments. In studies applied to planetary magma oceans, reducing conditions require the use of AuPd, Pt, or graphite capsules (e.g., Bernadou et al. 2021; Dalou et al. 2017; Grewal et al. 2019). In IHPVs, double capsules with external AuPd or Au capsules and internal Pt capsules have been developed to control and monitor

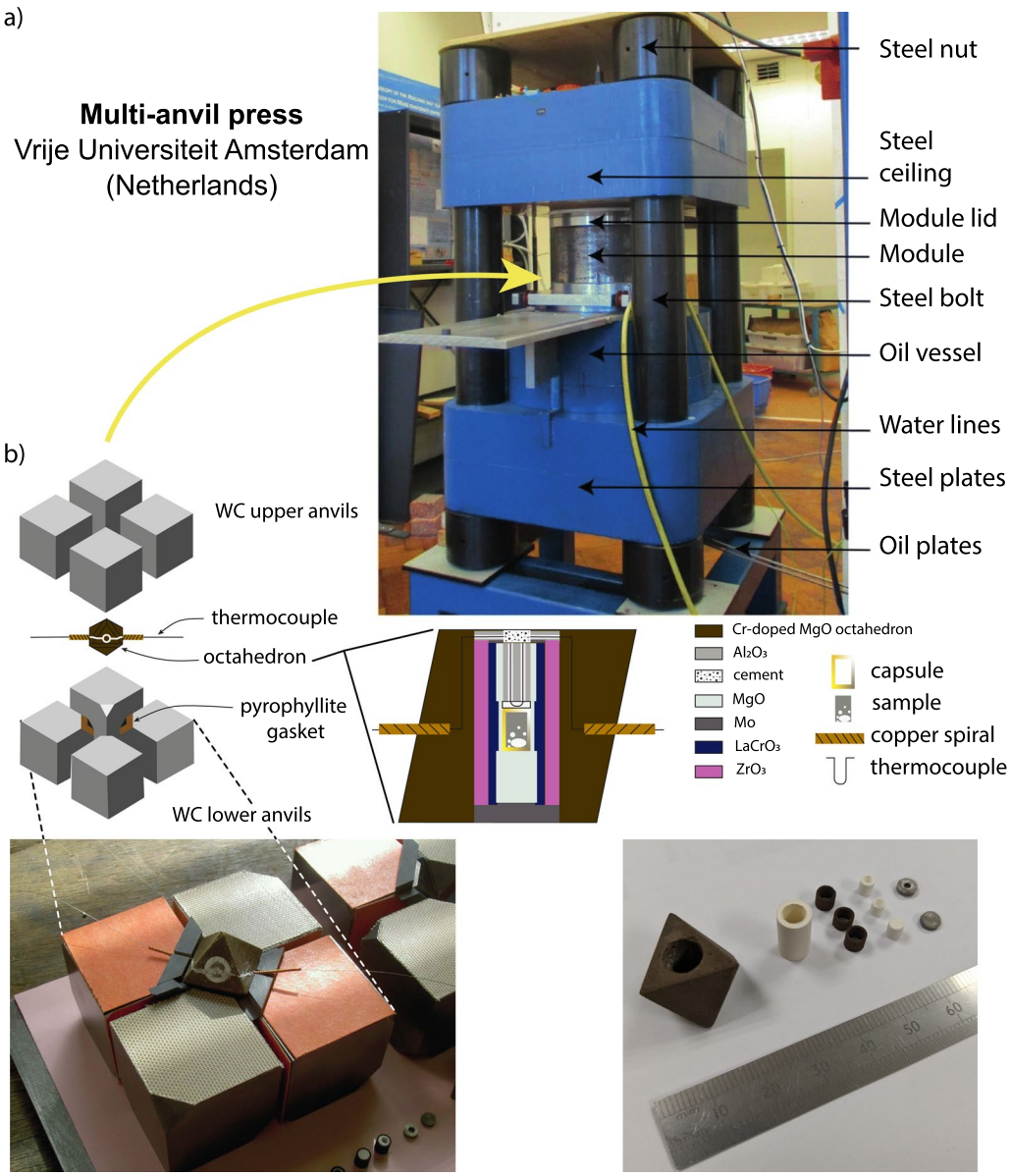

Fig. 6 **a** Photograph of the multi-anvil press installed at the Vrije Universiteit (Amsterdam, Netherlands), modified from Knibbe et al. (2018). **b** Schematic of the multi-anvil press secondary anvils, and a schematic and photographs of the assembly (courtesy of Pierre Condamine). Note that at the interface between the pressure medium and the pyrophyllite gasket, the copper coil around the thermocouple may significantly affect the electromotive force (EMF) of the thermocouple. Specifically, the nominal temperature is estimated to be ~ 150 K lower than the nominal temperature without a copper coil (Nishihara et al. 2006)

hydrogen and oxygen fugacities during experiments (e.g., Wilke and Behrens 1999). In piston cylinder and multi-anvil press experiments, graphite capsules or double Pt-graphite capsules (i.e., inner graphite and outer Pt; e.g., Armstrong et al. 2015) are often used to prevent Fe loss to the metal containers, ensure reducing conditions, and achieve high temperatures approaching planetary magma ocean conditions. However, graphite capsules are a source of C and lead to graphite-saturated conditions that yield C-saturated metal alloys. They are also more or less porous depending on their density, which often results in volatile losses (e.g., Grewal et al. 2019; Dalou et al. 2019a). Single-crystal olivine, pure forsterite, or MgO capsules can be used as alternatives, but the increasing dissolution of MgO with increasing experimental temperature (Fichtner et al. 2021; Dalou et al. 2022) must be considered when selecting starting materials.

3.1.4 Experimental designs

To study the metal–silicate partitioning of volatile elements, starting materials are silicate gels or mixtures of oxide powders considered analogous to a magma ocean composition and a core-forming metallic alloy composition. As magma ocean analogs, tholeiitic, primitive basaltic, or magnesian basaltic compositions are generally chosen (e.g., Kuwahara et al. 2019a; Grewal et al. 2019; Fichtner et al. 2021; Blanchard et al. 2022). In the case of multi-anvil presses, the high quench rate allows the use of chondritic and/or peridotitic compositions that are closer analogs to magma oceans (Roskosz et al. 2013; Boujibar et al. 2014), although it remains difficult to quench those compositions without forming olivine dendrites unless modifications to the standard design are made (see Bondar et al. 2021). Core-forming alloys are generally either solely iron or an iron–nickel mixture (Roskosz et al. 2013; Grewal et al. 2019) that may include, as discussed in the following section, a mix of iron carbide, sulfide, or nitride and iron monosilicide (e.g., Boujibar et al. 2014; Grewal et al. 2019). However, the choice of experimental design implies certain assumptions about Earth's accretion and core formation, as summarized in the following.

One procedure is to load a capsule with two separate phases: an iron alloy (Fe ± Ni, Si) containing the volatile elements of interest and a volatile-free (sometimes iron-free) silicate powder (e.g., Ballhaus et al. 2017; Grewal et al. 2021; Blanchard et al. 2022). The alloys are prepared by mixing pure metal alloys (Fe, FeS, $Fe_{83}Si_{17}$, Ni, Fe_4N, Fe_7N_3, etc.; e.g., Kilburn and Wood 1997; Dasgupta et al. 2013; Boujibar et al. 2014; Grewal et al. 2019; Jackson et al. 2021). A step to melt this mixture can be included; for instance, Blanchard et al. (2022) alloyed pure Fe with ^{13}C powder in a piston cylinder melting experiment at 2 GPa and 1873 K for 10 min in a MgO capsule. Once the metallic alloys are loaded into the capsule with the silicate powder and brought to the desired high-pressure and high-temperature (HP–HT) conditions, volatile elements equilibrate by diffusion from the metal alloy to the silicate phase, producing a large metallic pool (> 400 µm in diameter) on one side of the capsule and a large pool of silicate glass on the other (Fig. 7a). This procedure is ideal for physically and chemically separating fragments of silicate glass from the metal for bulk analyses by inductively coupled plasma mass spectrometry (ICP-MS) or gas mass spectrometry (see below). This design assumes that the core formed from large metal fragments that resulted from the accretion of large differentiated planetesimals and planetary embryos (Kleine and Rudge 2011). In this case, HVEs are already partitioned into the metal fragments and partially re-equilibrate with the surrounding silicate (magma ocean).

Alternatively, following the continuous accretion model (e.g., pebble accretion), the accreting metals form droplets small enough to equilibrate with the surrounding magma ocean (Kleine and Rudge 2011). To experimentally simulate the processes approximated in this model, volatile elements and a Fe-bearing silicate powder representing the magma ocean are loaded into the capsule with a reducer (e.g., Si or Fe metal). For instance, hydrogen can be added to the starting silicate powder as $Mg(OH)_2$ (e.g., Iizuka-Oku et al. 2017), $Al(OH)_3$ (Clesi et al. 2018), or synthesized water-bearing silicate glass (e.g., Tagawa et al. 2021). For carbon, graphite capsules have been widely used as the carbon source (e.g.,

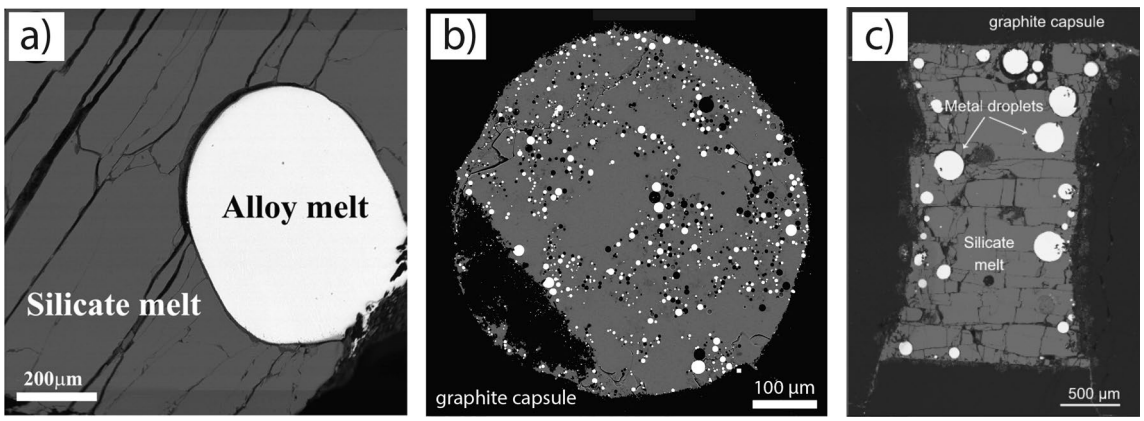

Fig. 7 Equilibrated metal–silicate samples produced in piston cylinder experiments. **a** Sample from Li et al. (2015) produced at 3 GPa, 1600 °C, and IW–4.8, by loading a volatile-bearing metal and a volatile-free silicate into the capsule (the single-stage core formation approach). **b** and **c** Samples from Dalou et al. (2017) synthetized at 3 GPa, 1600 °C, and IW–2.3, and from Speelmanns et al. (2018) synthetized at 1 GPa, 1250 °C, and IW–3.0, respectively, both produced by loading volatiles, Fe-bearing silicate powder, and a reducing metal into the capsule (the continuous accretion approach). See text for full descriptions of the two approaches

Dasgupta et al. 2013; Li et al. 2016; Dalou et al. 2017). To avoid C saturation in the metal phase, other types of capsules can be used (see previous section) and either graphite powder or vitreous carbon spheres added as the C source. For nitrogen, Si_3N_4 can be used both as a source of N and as a reducing agent (e.g., Roskosz et al. 2013; Speelmanns et al. 2019; Dalou et al. 2017, 2019a). Since its reduction potential is high, other sources of N, such as NH_4NO_3, have also been used (e.g., Li et al. 2016; 2023). In these experiments, because reduction occurs during heating, the metal segregates from the silicate at HP–HT. Hence, the equilibration of volatile elements between the metal and the silicate is controlled first by the reduction reaction and then by diffusion between the silicate melt and the metal alloy. This experimental procedure produces small metal blobs (10–80 μm in diameter) randomly distributed throughout the silicate glass (Fig. 7b, c; e.g., Speelmanns et al. 2019; Dalou et al. 2017, 2019a), unless the experiments are sufficiently long (≥ 6–12 h) to allow metal blobs to sink and coalesce into larger blobs (> 150 μm). However, such long experiments are often affected by volatile losses through the capsule (e.g., Dalou et al. 2019a).

In both cases, metal–silicate experiments are run at least 50 °C above the silicate liquidus (e.g., Dalou et al. 2017; Grewal et al. 2019), and experiments of both protocols are performed at similar temperatures. Assuming that chemical equilibrium is attained during the experiment, both of the above experimental approaches produce equivalent results. For instance, similar nitrogen partition coefficients between metal and silicate phases were reported by Grewal et al. (2019, 2021) using the first protocol and by Dalou et al. (2017) and Speelmanns et al. (2019) using the second protocol.

3.1.5 Attainment of chemical equilibrium

Chemical equilibrium must be assessed before publishing solubility or metal–silicate partitioning data. The first argument to support chemical equilibrium for an experimental sample is the compositional homogeneity of the phases (glass and metal) with respect to major elements and the investigated volatile(s) (H, C, N, and/or S) when measured by local analyses (see analytical section). The second argument is to perform time series experiments (i.e., experiments of variable durations): partition coefficients correlate with run duration below a certain run duration but remain stable over longer durations, suggesting a steady state has been reached. If independent tests yield similar results, this steady state can be equated with the attainment of equilibrium. Owing to the differences in diffusivities, the characteristic equilibration time differs for each element and varies with experimental conditions, such as P–T, fO_2, and phase compositions. However, elements may not necessarily diffuse in their elemental (monatomic) form, but rather as moieties (see Richter et al. 2009); diffusivities thus also reflect speciation, which is itself a function of P–T–X (e.g., Boulliung et al. 2021). Despite the relative ease with which time series can be performed, few are reported for metal–silicate experiments involving the equilibration of highly volatile elements (e.g., Shi et al. 2022 for N). Instead, the diffusivities, expressed in cm^2/s, of larger, heavier elements (mainly Si, Mg, and O in silicates or Fe and C in metals) are often used to calculate characteristic diffusion distances in comparison to the sizes of the samples or the phases (e.g., Malavergne et al. 2019). The argument here is that if larger and heavier elements (i.e., with theoretically slower diffusivities) are equilibrated in a sample synthesized at a certain duration, so must be smaller and lighter elements. Nonetheless, reversal experiments remain the most robust test of equilibrium; they are typically performed by varying the form in which starting materials are added to the experimental charge and ascertaining whether the same experimental product is produced. Finally, when partitioning or solubility data already exist in the literature at similar conditions to those being investigated, chemical equilibrium can be assessed by comparison with previous studies.

3.2 Laser-heated diamond anvil cell (LHDAC) experiments

LVPs produce samples large enough to be analyzed by bulk or local analytical methods, allowing for numerous and various types of structural, chemical, and vibrational analyses (see Sect. 5). As summarized above, thermodynamical parameters such as pressure, temperature, and oxygen fugacity can be controlled with relative precision using those experimental techniques. However, none of those methods can achieve the average P–T conditions relevant to metal–silicate equilibration during Earth's core formation (i.e., ≥ 45–55 GPa and ≥ 4000 °C; Bouhifd and Jephcoat 2011).

To determine metal–silicate partition coefficients at conditions relevant to core–mantle segregation in a deep magma ocean, experiments are also performed in LHDACs, in which materials are compressed between the truncated tips of two diamonds to pressures of 30–100 GPa and heated by an infrared (IR) laser to temperatures of 3000–6000 °C (Siebert et al. 2012; Fischer et al. 2015; Bouhifd and Jephcoat 2011). Starting materials are usually thin foils of iron alloyed with trace elements of interest and a pellet of powdered silicate/oxide mixture (e.g., basalt, peridotite, pyrolite compositions). Using a needle or other micromanipulator, these are placed in a pre-indented gasket sample chamber that is, in turn, placed between the two diamonds, and the pressure is increased by squeezing the diamonds' tips together via tightening

screws (Fig. 8a). Although rhenium or stainless steel are commonly used, various gasket materials have been employed, such as diamond, beryllium, boron (Lin et al. 2003), or a combination of Kapton, amorphous boron, and epoxy (Merkel and Yagi 2005). The choice of gasket is important because it determines the maximum attainable pressure, sample thickness, and the stress conditions within the sample (Merkel and Yagi 2005).

Many factors control the ability of DACs to generate pressure, but the simplest parameter is the diameter (d) of the diamonds' culets. O'Bannon et al. (2018) found that the maximum pressure a DAC can reach varies linearly with $d^{-0.54}$. For more details on the relationship between anvil geometry and achievable pressure, the reader is referred to O'Bannon et al. (2018). Pressure in the experimental chamber is determined before and after the experiments based on either the fluorescence of a small ruby placed near the edge of the chamber (Mao et al. 1978; Eggert et al. 1989; Dewaele et al. 2004) or the high-wavenumber edge of the diamond band in Raman spectra (Eremets et al. 2023). Uncertainties on these pressure measurements range between 5 and 10 GPa (Eremets et al. 2023). A thermal pressure correction is applied to the pressures measured after heating (Yen et al. 2020).

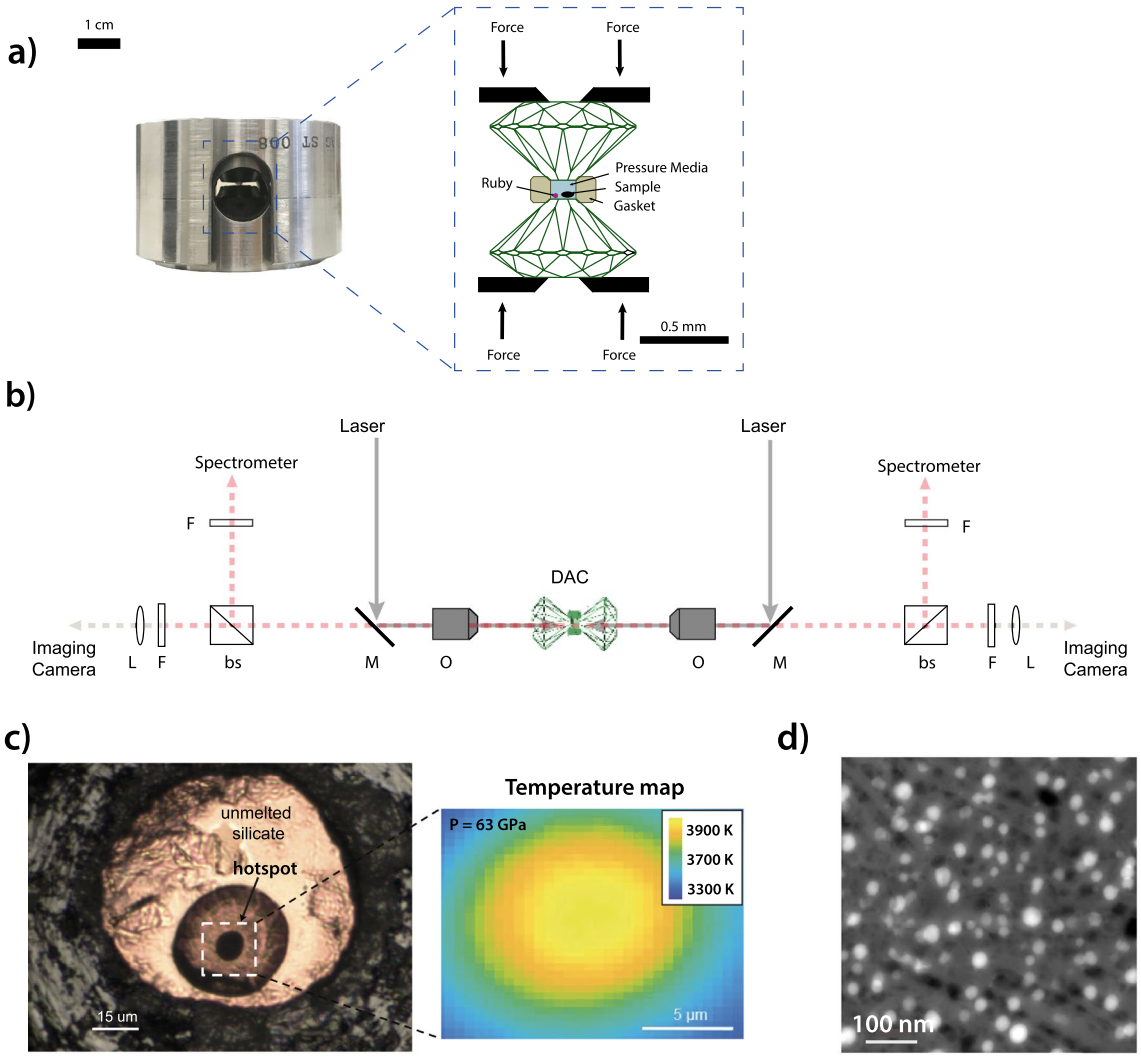

Fig. 8 **a** Photograph of a diamond anvil cell (DAC) with a cross section of the region hosting the experimental sample, modified from Yang and Zhaohui (2011). **b** Simplified schematic of a two-sided laser-heated system. Laser is directed by mirrors (M) to the two sides of the DAC. Thermal emission is directed via beam splitters (bs) to spectrometers to determine temperature. An objective collects an image which is focused by lenses (L) onto a camera. The DAC is usually illuminated by a white light source (not shown). Filters (F) are used to block unwanted wavelengths or reduce intensity. **c** Top-down view through diamond of a metal–silicate partitioning experiment after laser heating (the dark region indicates where the sample was molten) and a 4-color temperature map of the sample collected during laser heating (courtesy of T.A. Suer). **d** Small metal grains in the quenched silicate of the same sample, from Suer et al. (2017)

The optical transparency of the diamond anvils allows lasers to be used to heat the samples to high temperatures (Fig. 8b; Boehler 2000; Anzellini and Boccato 2020). Laser heating systems vary in design and capabilities, but generally consist of one or two IR lasers applying controlled heating to the material held between the two diamonds. CO_2 or YAG lasers with powers ranging from 50 to 200 W and peak wavelengths of 1064–1094 nm are typically used. The beams are collimated, directed, and focused into the sample chamber using suitable mirrors and lenses (e.g., Fig. 8b). Laser spot sizes can vary from 10 to 50 μm in diameter, and the temperature of the sample is raised by increasing the laser power. Images of the sample (typically magnified 10–20 times) and its thermal radiation are collected by a CCD camera and spectrometer, respectively. Thermal emission spectra from the heated region are recorded from one or both sides of the experiment and temperatures are extracted by fitting to a Wien or Planck function (Benedetti and Loubeyre 2004; Heinz and Jeanloz 1987; Walter and Koga 2004). Thermal emissions are collected by monochronometers in some studies, but multi-wavelength 2-D images can also be obtained from the heated region (Fig. 8c; Du et al. 2013; Campbell 2008; Lord et al. 2014).

Two major sources of uncertainty in laser heating studies are chromatic dispersion from refractive optical components and strong temperature gradients. Detailed discussions of how chromatic dispersion affects extracted temperatures and recommendations for reducing these effects are available in Walter and Koga (2004) and Benedetti and Loubeyre (2004). Through careful characterization of the experimental components and using consistent calibration standards, temperature uncertainties can be reduced to a few percent. Characterizing the wavelength dependent emission and absorption of materials used in the experiments under pressure can further help to ensure accurate temperature determination (Deng et al. 2017). A source of further uncertainty in temperature determinations, particularly for polyphase samples, is Mie scattering of the thermal emissions when passing between grains and phase boundaries (Lobanov et al. 2021). This effect can lead to uncertainties as large as ≥ 1000 K and should be considered when extracting temperatures in future partitioning studies.

The sample region at the focus of the laser heats up by absorbing laser energy until molten. If the sample is simultaneously probed by X-ray diffraction during heating, melting can be detected by disappearance of diffraction peaks or diffuse scattering (Yang 2016). For off-line experiments, changes in sample appearance from the motion of the melt or plateauing/leveling off of temperature have been used to detect melting although these methods can be imprecise (Andrault et al. 1998; Fiquet et al. 2010; Yang 2016; Yang and Li 2016). In metal–silicate experiments, the IR laser couples with the metallic part of the sample. Prolonged exposure to the IR laser anneals the silicate and metal phases into well-defined regions, as reflected by the morphologies produced in many metal–silicate partitioning experiments (e.g., Bouhifd and Jephcoat 2011; Siebert et al. 2012; Fischer et al. 2015; Suer et al. 2017; Blanchard et al. 2022). Shutting off the laser power rapidly quenches the experiments within microseconds, such rapid quench rates typically lead to glass formation which is thought to lock in equilibrium composition attained during melting. However, large amounts of H cannot be retained in the metal phase upon quenching and thus exsolve as bubbles, forming particular metallic quench textures (Okuchi 1997; Okuchi and Takahashi 1998).

During the laser heating partitioning experiments, samples can be heated continuously for a few to several tens of seconds. According to Fick's laws of diffusion, these timescales are long enough for chemical equilibration to occur for most species across the length scale of the molten hotspot (Corgne et al. 2008). Although the sample is completely molten under the focus of the laser, its outer regions remain solid and steep temperature gradients can occur during heating (Deng et al. 2017). Therefore, the size of the sample is of critical importance. The temperature in the middle of the hotspot can be considered to be homogenous, although thermal gradients become large away from the center. Temperature gradients drive chemical diffusion through the Soret effect, which can cause chemical zoning in experiments on molten silicates (Prescher et al. 2014; Sinmyo and Hirose 2010). The ratio of a specie's charge to its ionic radius determines its behavior along a thermal gradient. Therefore, the spatial distribution of major and trace species can be used to assess the degree of diffusion in metal–silicate partitioning experiments. Many studies have reported compositional homogeneity of major and trace species in both the metal and silicate phases of experiments as an indication of minimal thermal gradients. However, ascertaining such chemical homogeneity on the small spatial scale of the samples (tens of microns) is challenging, and further investigations by microanalytical techniques such as nanoscale secondary-ion mass spectrometry (NanoSIMS), transmission electron microscopy (TEM), and/or atom probe tomography (ATP) are needed.

3.3 Controversies surrounding partitioning measurements

Despite recent advances, measurements of volatile element partition coefficients remain controversial. Quench textures in both LVP and DAC experiments have been difficult to interpret, potentially resulting in inaccurately

reported trace element compositions and partition coefficients. Dendritic and quenched rim-overgrowth textures in LVP samples make it difficult to determine the equilibrium composition of the quenched liquid. Microscale and nanoscale metal-rich inclusions in the silicate have been difficult to assess with volumetric techniques such as electron probe microanalysis (EPMA) and can therefore complicate the interpretation of silicate trace element compositions. Analyses at higher spatial resolution, such as TEM imaging (Blanchard et al. 2022), have provided evidence of two distinct populations of metallic inclusions in the silicate glass: (1) large, irregularly dispersed inclusions up to several hundred nanometers in diameter (Fig. 8d), and (2) much smaller, uniformly dispersed inclusions a few tens of nanometers across. The larger population can be observed by scanning electron microscopy (SEM) and Blanchard et al. (2022) reported compositions similar to the largest metallic blobs in their samples, suggesting that they formed at high temperature, contrary to previous assumptions (Fischer et al. 2020). The presence of these larger metallic inclusions is a critical problem for determining HVE contents in silicate glasses because they may lead to overestimated contents of those siderophile elements in the silicate melt. For instance, Fischer et al. (2020) analyzed large areas of silicate glass including such "large" metallic inclusions because they considered the inclusions to have resulted from the quench, and thus that they would have been dissolved in the silicate at high *P–T*. However, Blanchard et al. (2022) avoided such "large" inclusions when analyzing their silicate glasses and obtained C partition coefficients one order of magnitude higher than those of Fischer et al. (2020) at comparable *P–T* conditions.

Although peridotitic or pyrolytic glasses are often used as magma ocean analogs, their high magnesium contents promote the growth of dendrites during quenching. In comparison, the use of basaltic or andesitic melts improves the homogeneity of the glass because they are more easily quenchable (e.g., Blanchard et al. 2022).

The loss of volatile elements from quenched experimental samples is another factor that can affect these measurements. Hydrogen has been particularly difficult to measure in experiments because its small atoms tend to escape the sample during quenching. Indeed, hydrogen may escape from samples prior to measurements upon decompression; FeH_x is known to decompose into body-centered cubic Fe and molecular H_2 (Iizuka-Oku et al. 2017). In addition, Clesi et al. (2018) and Malavergne et al. (2019) conducted carbon-saturated experiments, leading to carbon enrichment of the metal, which may hinder hydrogen incorporation (Tagawa et al. 2021). The presence of quench minerals in silicate glasses produced in LVP experiments (Clesi et al. 2018; Malavergne et al. 2019) are also problematic because of the structural difference between melt and mineral, which likely causes a loss of incompatible volatile elements from the melt. Therefore, reported hydrogen partition coefficients vary by more than an order of magnitude at the same conditions (Okuchi 1997; Clesi et al. 2018; Malavergne et al. 2019; Tagawa et al. 2021). Nevertheless, recent analyses combining EPMA, nuclear magnetic resonance spectroscopy, and elastic recoil detection analysis (ERDA) provided valuable data for hydrogen partition coefficients (Clesi et al. 2018; Malavergne et al. 2019).

Volatile concentrations added to the starting materials of some experiments can be much higher than those measured in natural samples. Such high concentrations violate Henry's law, leading to large uncertainties on reported partition coefficients for C (Kuwahara et al. 2019b; Grewal et al. 2021) and N (Shi et al. 2022; Grewal et al. 2022). Indeed, some elements are even saturated in the quenched silicate.

Finally, differences in the results of regression models used to fit measured HVE partition coefficients have been observed between the *P–T* ranges of LVP and DAC experiments. Evolving chemical tendencies in these distinct thermodynamic regimes may be responsible for these varied trends, and single linear functions are probably not sufficient over such large *P–T* ranges. Moreover, although fO_2 can also strongly affect these measurements, it is not always accurately accounted for.

4 Controlling and determining fO_2 during experiments

The oxygen fugacity of a magma ocean is a fundamental parameter for understanding the early evolution of a terrestrial planet because it controls the speciations and solubilities of volatile elements, their partitioning during core formation (siderophile *versus* lithophile), and their degassing into the primitive atmosphere (lithophile *versus* atmophile). Therefore, it is essential to accurately control and/or determine fO_2 in experimental petrology. Several techniques have been developed to control fO_2 in HP–HT experiments depending on the type of apparatus used. This section describes the *ex situ* determination of fO_2 in experimental samples containing metal, or, in the absence of any metallic phase, using Mössbauer or X-ray Absorption Near-Edge Structure (XANES) spectroscopy.

4.1 From metal–silicate equilibrium

The effect of fO_2 on the solubilities of volatile elements in reduced silicate melts can be investigated in a vertical furnace at atmospheric pressure by controlling the mixture of CO-CO_2 or N_2-CO-CO_2 gases supplied to

the atmosphere during the experiment (e.g., Boulliung et al. 2020). To reach very low oxygen fugacities, graphite crucibles can be used to reach fO_2 conditions at or more reduced than the C/CO buffer (i.e., IW − 6.6 at 1 atm and 1425 °C, reported in log units relative to iron–wüstite, i.e., Fe–FeO, equilibrium, IW) according to the reaction $C_{graphite} + 1/2\ O_{2gas} = CO_{gas}$. The C/CO buffer is reached when pCO is ~ 1 bar at total pressure $P_{total} = 1$ bar, which is usually the case in vertical furnaces. To lower this fO_2, it is possible to add an inert gas (rare gases, N_2, or others depending on the study) to decrease pCO by diluting the CO gas (Libourel et al. 2003). For instance, Libourel et al. (2003) performed experiments at different fO_2 while using graphite crucibles under variable nitrogen partial pressures of $0.05 < pN_2 < 0.95$ atm.

Under most conditions, fO_2 can be monitored during the experiment using a zirconia oxygen probe ($SIRO_2$ C700 + solid zirconia electrolyte oxygen sensor) with an uncertainty of ± 0.1 log units. In IHPVs, fO_2 can be flexibly controlled by admixing CH_4 or H_2 with the Ar pressure medium to impose the desired fH_2, and hence also fO_2 in hydrous experimental charges (Gaetani and Grove 1997; Moore and Carmichael 1998; Cottrell et al. 1999; Zajacz et al. 2010, 2011, 2012; Pichavant et al. 2014). Under anhydrous conditions, graphite capsules or sintered forsterite capsules can also be used to reach low fO_2 (Namur et al. 2016).

The most common method to vary (not control) oxygen fugacity in piston cylinder and multi-anvil apparatuses is to use metal buffers in addition to graphite, olivine, or forsterite capsules; this approach allows the maintenance of low fO_2 conditions during experiments and prevents the loss of iron, contrary to metallic alloy capsules such as Pt (e.g., Grove 1982). Graphite capsules are commonly used to buffer the fO_2 near the C/CO buffer via the reaction:

$$2FeO_{silicate} + C_{graphite\ capsule} = 2Fe_{metal} + CO_{2gas}. \quad (18)$$

Fichtner et al. (2021) used both San Carlos olivine and pure single-crystal forsterite (Fo) as capsules. Whereas Fo capsules can be considered as inert (to the first order), olivine capsules buffer fO_2 via the reaction:

$$Fe_2SiO_{4olivine\ capsule} \leftrightarrow 2\ FeO_{silicate\ melt} + SiO_{2silicate\ melt}, \quad (19)$$

by maintaining the FeO content of the silicate melt, thus preventing the sample from reaching very low fO_2 conditions.

The coexistence of a metal and its oxide at equilibrium constitutes an oxygen buffer, and can be used to control fO_2 during HP experiments, or to determine fO_2 in quenched samples (e.g., Cottrell et al. 2009; Burkemper et al. 2012; Dalou et al. 2017; Grewal et al. 2019; Blanchard et al. 2022). The common oxygen buffer relevant to early terrestrial planets is IW, which is often used to control and measure fO_2 in Fe-bearing experiments, including metal–silicate partitioning experiments. Iron or silicon metal are most often used to lower oxygen fugacities via the equilibria:

$$Fe_{alloy} + 1/2\,O_2 = FeO_{silicate\ melt} \quad (20)$$

$$Si_{alloy} + O_2 = SiO_{2silicate\ melt} \quad (21)$$

whereas specific capsules can be used in LVPs to target a range of fO_2 conditions, in DAC experiments, the diamonds impose the fO_2 within the chamber. Fe and/or Si metal can be added to DAC experiments, but they change the composition of the system (e.g., Fischer et al. 2015). In both LVPs and DACs, carbides (Fichtner et al. 2021), nitrides (Dalou et al. 2017; Speelmanns et al. 2019; Jackson et al. 2021), or sulfides (Namur et al. 2016; Labidi et al. 2016; Suer et al. 2017) are also commonly used because they act both as a source of volatile elements and reducers via reactions such as:

$$6\,FeO_{silicate\ melt} + Si_3N_{4nitride} = 6\,Fe_{alloy} + 3\,SiO_{2silicate\ melt} + 2\,N_{2silicate\ melt\ or\ alloy}. \quad (22)$$

After experiments, the intrinsic oxygen fugacities of quenched samples are calculated from thermodynamic modeling of Fe–FeO equilibrium (Eq. 20) between metallic and silicate glasses based on electron microprobe analyses and expressed relative to IW. Following this equilibrium, fO_2 can be calculated from the Fe and FeO concentrations of coexisting alloy and silicate melt via the relation (Médard et al. 2008):

$$\log_{10} fO_2 = \frac{2}{\ln(10)}\left[\ln\left(\frac{X_{FeO}^{melt}}{X_{Fe}^{alloy}}\right) - \ln\left(\gamma_{Fe}^{alloy}\right) + \ln\left(\gamma_{Fe}^{melt}\right) - \ln K\right] \quad (23)$$

where X_{FeO}^{melt} and X_{Fe}^{alloy} are the mole fractions of FeO and Fe in the silicate melt and the metal alloy, respectively, calculated on a cation basis, γ_{FeO}^{melt} and γ_{Fe}^{alloy} are their respective activity coefficients, and K is the equilibrium constant of the reaction calibrated by Médard et al. (2008). γ_{FeO}^{melt} is assumed to be unity in an ideal solution model, but values up to 1.7 have been used to model non-ideal solutions (Holzheid et al. 1997). This difference would shift the ΔIW value by ± 0.46 log units (Speelmanns et al. 2019). The effects of other components (e.g., C, N, Si, P, S, or Ni) on γ_{Fe}^{alloy} are accounted for using a derived version of the "Wagner ε formalism" (Wagner 1962; Ma 2001) for non-ideal interactions in liquid Fe alloys, following the approach and formulation of Wade

and Wood (2005) and utilizing the calculator provided at http://www.earth.ox.ac.uk/~expet/metalact/. To allow direct comparison to the IW buffer, the activity of Fe can be adjusted following the method of Stanley et al. (2014). Whereas the stable liquidus phase of solid Fe is δ-Fe at high pressure, the IW buffer is calibrated for γ-Fe (see references in Stanley et al. 2014). Therefore, the activity of Fe in the alloy, a_{Fe}^{alloy}, must be correct for both (1) the difference in the entropy of fusion (ΔS) of the stable phase of Fe at experimental conditions (γ-Fe; extrapolated from Desai 1986) and that of the stable liquidus phase (δ-Fe), and (2) the temperature difference between experimental temperatures (T) and the extrapolated fusion curve of gamma-Fe (T_L; Andrault et al. 2009) to obtain the activity of Fe in *HP–HT* liquid alloys as:

$$a_{Fe}^{\gamma\text{-Fe}} = a_{Fe}^{alloy} + \exp\left(\frac{\Delta S(T - T_L)}{RT}\right), \quad (24)$$

where R is the ideal gas constant and temperatures are in kelvin. The resulting fO_2 value calculated from Eqs. (23) and (24) is then compared to the IW buffer corrected for pressure effects following Zhang et al. (2016).

Under very reduced conditions (< IW–4), FeO is no longer present in silicate melts at weight percent concentrations. In this case, fO_2 is also calculated from Si–SiO_2 equilibrium as described by Cartier et al. (2014).

However, in some cases, metal blobs are too small to be analyzed. In samples loaded in AuPd and Pt capsules, palladium and iridium powders can also be mixed with the starting products to create Fe–Pd and Fe–Ir alloys as fO_2 sensors in the capsules (Bernadou et al. 2021). In such cases, the activity coefficients of iron (γ_{Fe}) for the Fe–Ir and Fe–Pd alloys are determined using Woodland and O'Neill's (1997) equation and taken from Aukrust and Muan (1962), respectively. Bernadou et al. (2021) calculated fO_2 using both methods (i.e., the capsule alloys vs. the activity coefficients of FeO in the silicate melt and Fe in the metal alloy) and compared the results to check for internal consistency and validate their attainment of equilibrium; they obtained differences between 0.1 and 0.4 log units.

4.2 In the absence of metal

In samples with no metallic phase, it is fundamental to the redox state of multivalent elements to probe the samples' fO_2. Because Fe is the most abundant multi-valence element in the mantles of terrestrial planets, knowledge of its valence state is important for understanding oxygen fugacity in the absence of metals. Nonetheless, some experiments can be performed with Fe-free compositions to study the evaporation or solubility of siderophile elements (e.g., Dalou et al. 2022). In that case, the redox state of other transition metals such as Ti, Eu, V, Cr, or Ni can be used as a proxy to determine a sample's fO_2.

4.2.1 *Mössbauer spectroscopy*

Mössbauer spectroscopy is a well-established, non-destructive technique mostly used in the Earth sciences to investigate the redox states of elements with Mössbauer-sensitive isotopes in solid media. It provides information on the electronic environment around the nuclei of those isotopes, through which it is possible to determine their valence (i.e., redox state), site occupancy, distortion of the coordination environment, spin state, and magnetic properties (Bancroft et al. 1967; Gütlich et al. 1978; Burns and Solberg 1990).

Samples amenable to the collection of Mössbauer and XANES (described below) spectra can be produced by experimental techniques including, but not limited to, those mentioned above. The quantity of ^{57}Fe is a limiting variable for Mössbauer spectroscopy given its low natural abundance; therefore, experimental samples are often doped with ^{57}Fe. In contrast, the quality of XANES spectra is insensitive to the proportions of the isotopes of iron. For both methods, different sample preparation techniques (polished surface, sample thickness, or bulk powder) are possible and depend on the beamline.

The Mössbauer effect is based on the recoilless emission and absorption of γ-rays during nuclear transitions between the ground and excited states of certain nuclei in a solid (Mössbauer 1958). Despite H, C, N, and S not having any Mössbauer-active isotopes, the redox state of silicate glasses can be determined by investigating the 14.4 keV transition of ^{57}Fe. Studies of ^{57}Fe represent more than 95% of all Mössbauer applications (McCammon 2003), with the remainder being limited to other common Mössbauer-active isotopes such as ^{119}Sn (e.g., Gütlich et al. 1978; Roskosz et al. 2020).

Today, Mössbauer spectroscopy, alongside wet chemistry and XANES spectroscopy, is one of the most widely used techniques for determining $Fe^{3+}/\sum Fe$ in solids (Dyar et al. 2006). Its quantification is based on the deconvolution of the Mössbauer spectrum into one or more subspectra (McCammon and Kopylova 2004), from which the relative areas and hyperfine parameters (i.e., central shift, quadrupole splitting, and hyperfine magnetic splitting) of each subspectra can be obtained. Beyond the Curie or Néel temperature, the Mössbauer spectra of paramagnetic materials, such as silicate glasses, are characterized only by the central shift and quadrupole splitting, resulting in Mössbauer spectra comprising two absorption lines (i.e., doublets; Fig. 9a). The range within which the central shift and quadrupole splitting occur enables the identification of the valence and spin

state (Bancroft et al. 1967). Moreover, in a crystalline solid, information on the coordination environment and site distortion are also obtained (Bancroft et al. 1967; McCammon and Kopylova 2004). However, below the Curie or Néel temperature, magnetic splitting is observed and Mössbauer spectra are characterized by six absorption lines (i.e., sextets) (McCammon 2000). The relative amount of each subspectrum (i.e., site) is determined by its area compared to the total Mössbauer spectrum area. Hence, high spectral resolution is crucial, especially for silicate glasses, which are characterized by (1) the symmetrical broadening of initially Lorentzian line shapes into Gaussian distributions that reflect the occupation of Fe in a variety of different sites, and (2) their lack of long-range order (Jayasuriya et al. 2004; Virgo and Mysen 1985; Yaroslavtsev and Chumakov 2022). The relative amounts of each oxidation state (i.e., Fe^{2+} and Fe^{3+}), as quantified by the areas of their corresponding doublets, also depend on the absorber-thickness effect (which depends on the number of Fe nuclei and the cross section of the sample) and the recoil-free fraction of each oxidation state (McCammon and Kopylova 2004). Variations in sample thickness or its thickness variability can alter the intensities of the absorption lines, potentially compromising accurate identification of existing species, especially when Fe^{3+} is present in minimal amounts in highly reduced materials. The recoil-free fraction of each oxidation state is a temperature-dependent parameter and differs between Fe^{2+} and Fe^{3+} (De Grave and Van Alboom 1991). Because the recoil-free fractions of both Fe^{2+} and Fe^{3+} approach 1 at low temperatures, several studies have performed analyses under liquid He (4 K) or liquid N_2 (77 K) to maximize the recoil-free fraction (e.g.Roskosz et al. 2020; Zhang et al. 2017), thereby avoiding overestimating the ferric iron content (De Grave and Van Alboom 1991).

Mössbauer spectroscopy can be conducted both at ambient and HP conditions, but not at high temperature owing to its effect on the recoil-free fraction. Compared to laboratory-based Mössbauer sources, the greater brilliance (and hence more rapid data collection) of synchrotron sources are crucial for precisely characterizing the redox states of silicate glasses, should the samples be limited by low ^{57}Fe abundance or small spatial extents (Potapkin et al. 2012). The spectrum collection time depends on the amount of ^{57}Fe, velocity range (mm/s), and temperature (McCammon 2021), typically taking ~ 1–4 h, compared to a few days using a conventional Mössbauer source for similar quality spectra. Additionally, the $Fe^{3+}/\Sigma Fe$ ratios from XANES spectra are quantified by comparing the spectra of unknowns (i.e., samples) to those of well-known standards, established via Mössbauer spectroscopy or wet chemistry (e.g., Berry et al. 2018; Cottrell et al. 2009). Indeed, Mössbauer calibrations show that the intensities of XANES spectral features, such as the centroid or edge energies, are not simple linear functions of $Fe^{3+}/\Sigma Fe$ in silicate glasses or other isotropic phases such as garnet (Berry et al. 2003; Wilke et al. 2004; Zhang et al. 2017), emphasizing the role of Mössbauer spectroscopy in determining the absolute $Fe^{3+}/\Sigma Fe$ ratios of solids.

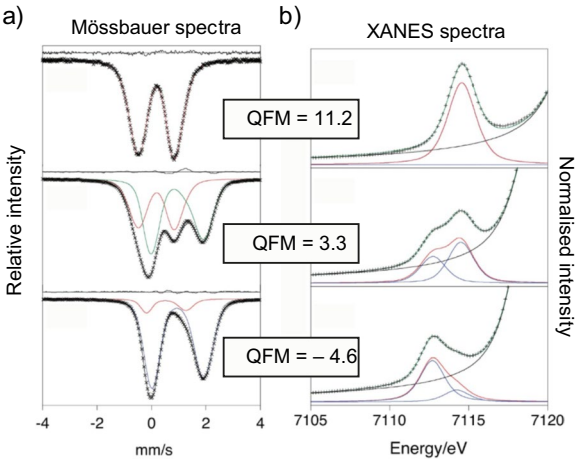

Fig. 9 Comparison between ^{57}Fe-enriched Mössbauer spectra (left) and the pre-edge region of the Fe K-edge XANES spectrum (right) of MORB glasses (synthesized and equilibrated at 1400 °C and indicated fO_2 conditions relative to the QFM buffer) analyzed at room temperature and pressure (modified from Berry et al. 2018). For theses glasses, ΔQFM + 11.2 corresponds to $Fe^{3+}/\Sigma Fe = 1$, ΔQFM + 3.3 to $Fe^{3+}/\Sigma Fe \approx 0.4$, and ΔQFM –4.6 to $Fe^{3+}/\Sigma Fe = 0$

4.2.2 *X-ray absorption near-edge structure (XANES) spectroscopy*

XANES is a non-destructive element-selective technique utilizing synchrotron radiation to generate X-ray photons of a specific energy (i.e., monochromatic) that are then absorbed by the material of interest to excite a core electron from an initial ground state to an unoccupied or continuum state above the Fermi level. The energy of the absorption edge corresponds to the core-level energy, which is characteristic for each element. Because of the capacity to characterize the electronic environment around *any* element, it has become widely popular in the Earth Sciences over the past ~ 30 years.

XANES spectra can be divided into three characteristic regions in order of increasing energy: the pre-edge, edge, and post-edge. Each region is used to determine a material property. The spectral shape in the pre-edge region of transition metals (e.g., Fe *K*-edge, Fig. 9b) is related to the transition from the 1 *s* core state to a bound state in the 3*d* shell (1 $s \rightarrow 3d$, the quadrupole transition). The strength of this transition is only 0.1% that of the dipole

transition, but, because of the high density of state for the 3*d*-band, small peaks (usually 1–3% intensity) are visible in most octahedral transition metal systems (Henderson et al. 2014). These peaks provide information about the electronic properties and local geometry of the absorbing atom, through which it is possible to determine its valence. In most instances (i.e., unless forbidden by selection rules), the edge region reflects the binding energy of a core level. The shift of the edge to higher energies with higher valence can be used to determine (but rarely to quantify) the valence of 3*d* transition metals in unknown systems. The extended X-ray absorption fine structure (EXAFS) region occurs at higher energies (post-edge) and provides information on the local geometric structure around the absorbing site. In this section, we focus only on the pre-edge and edge regions of XANES spectra.

By far the most widely used application of XANES in the Earth Sciences involves 1 *s* X-ray absorption (*K*-edges) of 3*d* transition metals, especially Fe in glasses and minerals (Bajt et al. 1994; Berry et al. 2003, 2018; Wilke et al. 2004; Cottrell et al. 2009). XANES spectra are not readily predicted via *ab-initio* simulations (although density functional theory simulations are becoming more sophisticated; see Jahn and Kowalski 2014), meaning that the redox state of iron (and those of other elements) are typically quantified by empirical means. Of these, the most widely used is to determine the relative intensities of the two pre-edge features, one at ~ 7112 eV and the other at ~ 7113.5 eV, by integrating the areas under the two curves (typically assuming either Gaussian or pseudo-Voigt functions) to yield the *centroid* energy (e.g., Wilke et al. 2001; Fig. 9b). The centroid energy can then be compared with those of standards with known Fe^{3+}/Fe^{2+} to determine that in the unknown. In most cases, the centroid energy varies in a non-linear fashion with Fe^{3+}/Fe^{2+} because the intensities of the peaks at 7112 and 7113.5 eV differ according to the symmetry of the site(s) in which Fe resides; lower symmetry sites (e.g., tetrahedral) induce higher intensity pre-edge features than centrosymmetric (e.g., octahedral) sites. Nevertheless, the merit of this approach is that the energies of the end-members remain fixed and are thus independent of coordination or composition (Wilke et al. 2001; Fiege et al. 2017). The reader is referred to Berry et al. (2003), Wilke et al. (2004), Cottrell et al. (2009), and Hawthorne and Waychunas (1988) for detailed discussions of peak and background fitting methods. This approach can achieve a precision of ± 0.02 on the $Fe^{3+}/\Sigma Fe$ ratio. Other methods involve using the shift in edge energy in tandem with the centroid (Berry et al. 2018), linear combination fitting, or whole-spectrum treatments that yield comparable results (± 0.036; Dyar et al. 2016). One point of warning is that the pre-edge intensity of *K*-XANES has a self-absorption issue, which affects the XANES spectrum (e.g., Berry et al. 2010). The effect of self-absorption leads to spurious attenuation of peak intensities (particularly that of the white line) and can be ameliorated by decreasing the effective thickness of the sample containing the element in question. This may be achieved by decreasing the path length of the X-rays interacting with the sample by collecting only fluoresced X-rays with detector(s) placed at an acute angle, or, if possible, diluting the sample through admixture with other, non-absorbing compounds, such as boron nitride or cellulose.

Other transition metals relevant to geological systems that have been measured in glasses by XANES are Ti (e.g., Cormier et al. 2011), Eu (e.g., Burnham et al. 2015), V (e.g., Sutton et al. 2005), Cr (e.g., Berry and O'Neill 2004), Co (e.g., Choy et al. 2001), Ni (e.g., Essilfie-Dughan et al. 2012), Cu (e.g., Berry et al. 2006), and Zn (e.g., Waychunas et al. 2003).

Because the treatment of XANES spectra does not yield absolute amounts of the species (largely redox state) in question, a set of standards with oxidation states precisely quantified by Mössbauer spectroscopy or wet chemistry is required to accurately quantify the proportions of redox pairs. Furthermore, because XANES spectra are sensitive to all aspects of the electronic structure of the target element, quantifying redox state requires that the element of interest in both the samples and standards be in the same coordination environment (Galoisy et al. 2001; Berry et al. 2003; Wilke et al. 2001; Cottrell et al. 2009). Moreover, as the photon fluxes of 3rd-generation and later synchrotron setups increase, spurious changes in oxidation state induced by interactions with the incident beam via electron transfer ('beam damage') have become prevalent. Both increases and decreases in mean valences have been reported (e.g., Ferreira et al. 2013), particularly for glasses with high water contents (e.g., Gaborieau et al. 2020). Because the probability for this transformation increases with time (i.e., with increasing integrated flux), the occurrence of beam damage can be ascertained by performing rapid scans (e.g., energy-dispersive) or sampling various points in a homogeneous sample at the energy at which the change in intensity is expected to occur. Finally, because the incident synchrotron radiation is polarized, the absorption intensities of anisotropic phases vary according to their orientation. Therefore, accurate determination of the bulk redox state of an anisotropic material requires characterization of redox state as a function of crystallographic axis (e.g., Steven et al. 2022).

Unlike Mössbauer spectroscopy, XANES is applicable to all natural states of matter, is relatively insensitive to temperature (often performed at high temperature; Neuville et al. 2014), and can be applied to a broader range of

elements including S (e.g., Métrich et al. 2009; Brounce et al. 2019; Lerner et al. 2021). These strengths enable XANES to provide a more comprehensive constraint on the fO_2 of a sample by comparing multiple redox-sensitive elements in the same phase. Consequently, XANES is the preferable choice for routine redox measurements in well-characterized systems given an element- and phase-specific calibration to prior determinations. Additionally, in systems with multiple redox-sensitive elements, electron exchange between two redox couples can occur upon quenching, the most well-studied example being that between Cr and Fe: $Cr^{2+} + Fe^{3+} = Cr^{3+} + Fe^{2+}$ (Berry et al. 2006; Cicconi et al. 2015).

5 Compositional analyses

The choice of analytical method is more often limited by the size or mass of the experimental sample than by the volatile element abundances in the phases. Indeed, starting materials for HP–HT experiments are often enriched in volatile elements at the wt.% level, and, despite variations of their partition coefficients and volatile losses through capsules, the concentrations of volatile elements in phases easily reach tens to hundreds of parts per million.

5.1 Bulk analyses

From IHPVs to DACs, the size of the sample chamber decreases from 60 mm to ≤ 100 µm in diameter, with associated consequences on the applicability of analytical methods. For instance, IHPV and piston cylinder samples are > 20 mg, allowing the metal and silicate phases to be separated manually and individually analyzed using bulk methods. After quenching and decompression, capsules are carefully opened or cut in half with a diamond wire saw. Metal and glassy silicate phases are then separated by hand under a binocular microscope, washed, and crushed to a fine grain size (50–150 µm). Nitrogen concentrations in silicate and metallic phases have been measured using elemental analyzers (Speelmanns et al. 2018, 2019) and by noble gas mass spectrometry (NGMS; Li et al. 2016; Mosenfelder et al. 2019; Dalou et al. 2019a; Boulliung et al. 2020). Both IRMS and NGMS require chemical separation followed my mass spectrometric analysis carried out with gas via magnetic sector mass spectrometry. Extraction and chemical separation techniques vary depending on the nature of the material and the targeted elements. Both analytical techniques require a filament-based source to ionize the gas, a vacuum system to maintain the ions, an analyzer for dispersing the ions according to their masses and charges, and a detection system (faraday cups or electron multipliers). The main difference between the two techniques lies in the vacuum system, which can be dynamic (IRMS) or static (NGMS). For IRMS, the sample and reference gases are introduced through a dual inlet to allow rapid comparison and normalization; hence, the gases are continuously leaked into the spectrometer and the system must be pumped dynamically. In contrast, for NGMS, the gas mass spectrometer is isolated from the vacuum pumping system and the gas is consumed during analysis. In addition, the gas is isolated cryogenically and introduced via a simple inlet. Another difference is that IRMS can measure the abundances of H, C, N, and S, whereas NGMS can only measure N abundances.

Those bulk absolute methods are advantageous because they do not require reference materials with similar matrices for calibration and they have reproducibilities < 2% (1σ) for samples with abundances exceeding 100 ppm (as in doped experimental samples). Several studies have measured N contents by NGMS in small pieces of both metal and silicate heated individually with a continuous-mode infrared CO_2 laser mounted on an x–y stage (Li et al. 2016; Dalou et al. 2019a), or within a furnace equipped with a tungsten wire (Shi et al. 2022). Repeated heating stages are used to verify that all N was extracted. The extracted gas is then purified to chemically remove active volatile species such as H_2, CH_4, H_2O, CO, and CO_2 before analysis by NGMS.

Sulfur concentrations in metallic and silicate phases have been analyzed by IRMS (Labidi et al. 2016), but this method requires a wet chemistry step to transform the S dissolved in phases into SF_6 gas for IRMS analysis. The advantage of this bulk method for S-bearing experimental samples is that it averages heterogeneities within the metallic phases that are present due to the immiscibility of C-rich and S-rich iron alloys. Although both NGSM and IRMS are very precise methods, NGSM can measure N concentrations at the ppm level to better than 10% precision in glass fragments of 0.4–2 mg or metal beads of a few micrograms (Dalou et al. 2019a; Boulliung et al. 2020), whereas IRMS requires hundreds to thousands of milligrams of material to measure C, N, or S concentrations with such precision. In addition, if sufficient moles of an element are present in the sample, such methods can also provide isotopic compositions.

5.2 Local analyses

Small experimental samples or multiphase samples with phases smaller than 50 µm require local analytical methods (Table 1). In such cases, recovered capsules from large-volume apparatuses are often cut in half using a diamond wire saw and one half is mounted into epoxy/resin, attached to a base using crystal bond or ethyl 2-cyanoacrylate ("superglue"), and polished with Al_2O_3 powder and ethanol.

Table 1 Comparison of the different analytical techniques used to perform chemical analyses of experimental run products

Technique	Spatial resolution	Detection limits	Uses
EPMA	≥ 1 µm	100 s of ppm	C, N, S
SIMS	≥ 10 µm	A few to 10 s of ppm	H, C, N, S
NanoSIMS	100 s of nm	A few to 10 s of ppm	H, C, N, S
LA-ICP-MS	10 s of µm	700 ppm	S
ERDA	10–100 s of µm	90 ppm	H, C
IR spectroscopy	10 s of µm	A few to 10 s of ppm	H, C
Raman spectroscopy	100 s of nm to a few µm	> 1000 ppm	H, C

5.2.1 Electron probe microanalysis (EPMA)

EPMA has been used to determine C, N, and S concentrations in experimental samples. This method has been applied to both LVP and DAC samples (e.g., Roskosz et al. 2013; Fisher et al. 2020), but is more commonly used for LVP samples. EPMA measures the characteristic X-ray intensities emitted by elements present in a sample when its surface is bombarded with a focused electron beam. For each element, the characteristic X-ray intensity emitted from the sample is normalized to that of a standard of known composition, and this normalization is referred as the k-ratio. The measured k-ratios are transformed into concentrations via analytical algorithms. Depending on the density of the material, the analytical area can be smaller than 1 µm by applying small accelerating voltage (e.g., 10 kV), although this remains difficult by EPMA. The compositions of 1-µm to submicron phases often have larger analytical uncertainties, suggesting contamination by adjacent phases (e.g., Ishii et al. 2023).

Because the detection limits are high for N and S (0.03 and 0.01 wt.%, respectively; von der Handt and Dalou 2016; Labidi et al. 2016), EPMA can only be used for highly doped samples. Carbon contents in metal alloys are often calculated by difference, but can be also measured by EPMA if the samples are not carbon coated (Boujibar et al. 2014). For instance, Dasgupta et al. (2013) coated their polished experimental samples with aluminum as a conductive coating, using stoichiometric Fe_3C and Fe_7C_3 as primary and second standards, respectively, to measure C in metallic melts. This method shows good agreement with C contents measured by SIMS (Dasgupta et al. 2013).

The advantage of EPMA is that it is not very sensitive to matrix effects; thus, reference materials do not need to have compositions extremely similar to those of the analyzed phases. For instance, stoichiometric cementite (Fe_3C, Boujibar et al. 2014), silicon nitride (Si_3N_4, Dalou et al. 2017) or iron nitride (Fe_2N or Fe_4N, Roskosz et al. 2013), and pyrite (FeS_2, Labidi et al. 2016) have been used to measure C, N, and S, respectively. In addition, C, N, and S can be analyzed alongside other major elements. In studies presenting metal–silicate partitioning data on C, N, and S, these elements are often measured in the silicate phase either by SIMS (or NanoSIMS) or EPMA, but the metal phases are most commonly measured by EPMA (e.g., Dalou et al. 2017; Suer et al. 2017). The main reasons are that (1) there are currently no metallic reference materials available to calibrate these measurements by SIMS, and (2) C, N, and S are often present at levels of thousands of parts per million or a few weight percent in the metal phases and are therefore easily measurable by EPMA. In contrast, as C, N, and S are siderophile over an extended range of experimental conditions, they are present at hundreds of parts per million in the silicate glasses, making them difficult to analyze by EPMA.

The main advantages of EPMA are (1) the ease of access in many laboratories, (2) high spatial resolution, (3) low analytical costs compared to other analytical methods, and, as mentioned before, (4) simultaneous determination of C, N, and S alongside other major elements.

5.2.1.1 Secondary-ion mass spectrometry (SIMS) The abundances of H, C, N, and S in silicate glasses are commonly determined by SIMS with detection limits at the ppm level and internal precision better than 5%, which is generally well below the standard deviation of the number of analyses performed in experimental samples (e.g., Dalou et al. 2017; Nash et al. 2019; Boulliung et al. 2020; Fichtner et al. 2021). This method can be applied to both LVP and LHDAC samples, but the large beam spot size (generally > 10 µm in diameter) have limited its use for LHDAC samples. It is therefore more suitable for LVP samples.

For SIMS analyses of H, C, N, and S, a focused primary ion beam of Cs^+ (an O^- beam would generate positive secondary ions) is used to ablate (or 'sputter') the surface of a polished sample, and the resulting secondary ions are extracted and transferred to a mass spectrometer for analysis. Whereas IRMS and NGMS require simple mass spectrometers with only a section magnet to separate

masses at high mass resolution because of the chemical separation procedures performed beforehand, there is no chemical separation procedure performed before SIMS analyses, so a high mass resolution is necessary to reduce interferences and separate molecular and atomic isobaric species. For instance, Füri et al. (2018) used a mass resolution ≥ 10,725 to separate the $^{15}N^{16}O^-$ peak from $^{29}SiH_2^-$ in N- and H-bearing silicate glasses, whereas a mass resolution of 600 was used in recent NGMS analyses of N, regardless of the detector (Boulliung et al. 2020). The key features of SIMS that allow the local measurement of ppm levels of H, C, N, and S in silicate glasses are (1) its high secondary ion yields, and (2) the extremely low background signals, facilitating high signal-to-noise ratios.

Measurements of volatile elements by SIMS require a certain sample preparation protocol to lower the background noise and increase the precision of the measurements, as follows. Samples must be removed from their resin mount, pressed into high-purity indium metal mounts, and gold-coated. Then, samples are generally left in an oven and/or a degassing bench for at least 24 h, and then in the instrument airlock for at least another 24 h to ensure the thorough removal of any adsorbed water before introduction into the sample chamber. In addition, prior to analysis, the surfaces of glasses and metals are pre-sputtered for 180 s over a minimum area of 10 µm × 10 µm to minimize any surface contamination. Because volatile abundances are determined using the calibrated relationship between the secondary-ion intensity ratios $^{16}OH^-/^{29}Si^-$,$^{16}OH^-/^{17}O^-$, $^{16}OH^-/^{18}O^-$, $^{12}C/^{18}O^-$, $^{14}N^{16}O^-/^{16}O_2^-$, and/or $^{32}S^-/^{30}Si^-$ and the known equivalent H_2O, CO_2, N, or S abundances in silicate glass reference materials, the reference materials must have major element compositions similar to those of the experimental silicate glasses. This method is well-developed and calibrated, and many laboratories around the world have analyzed H, C, and S for decades (e.g., Delaney and Karsten 1981; Pan et al. 1991; Hervig 1992; Deloule et al. 1995; Hauri 2002; Hauri et al. 2002*)*. In contrast, nitrogen analyses were only recently developed, and reference materials remain scarce (Regier et al. 2016; Füri et al. 2018; Mosenfelder et al. 2019). Nonetheless, the agreement between N analyses via SIMS and NGMS is very promising (Fig. 10a).

5.2.2 NanoSIMS

NanoSIMS can be used to analyze LVP samples (e.g., Gao et al. 2022), but remains the most common method for analyzing HVEs in DAC samples (e.g., Suer et al. 2017; Blanchard et al. 2022). Indeed, DAC experimental sample volumes (~ 0.0001 mm^3) are orders of magnitude smaller than those from multi-anvil experiments (~ 1 mm^3 for the smallest multi-anvil samples). Therefore, DAC samples require special preparation for analysis. After quenching and decompression, a cross section of the quenched melted region is recovered using a focused ion beam (FIB) instrument (Fig. 11a, b). These 1–5-µm-thick lamellae, usually of a 20 µm × 30 µm region, are polished by ion milling and placed on a suitable substrate for chemical analysis. More details on DAC sample preparation can be found in Jennings (2020). Recently, NanoSIMS has been used to image the relative abundances of C (Fischer et al. 2020; Blanchard et al. 2022) and S (Suer et al. 2017) in metal and silicate phases.

Although its fundamental principle is similar to SIMS, NanoSIMS has the ability to refocus a Cs^+ primary beam to ~ 50 nm in diameter, thereby combining fine spatial resolution with a sector mass spectrometer capable of isotopic analyses like SIMS. The advantage of NanoSIMS relative to standard SIMS analyses is the submicron lateral resolution, which is achieved by positioning the primary probe-forming lens parallel and very close to the sample, focusing the beam to a very small diameter. NanoSIMS analyses are performed in two steps: first, the sample is chemically imaged using a controlled raster of the primary beam across the sample surface to produce high-resolution ion maps for selecting a region of interest (1–5 $µm^2$); then, analyses are performed while avoiding cracks, grain boundaries, graphite inclusions, etc. However, using such a finely focused primary beam (of a few picoamperes) to sputter the sample surface results in secondary ion signals that are commensurately low, leading to lower precision than in conventional SIMS analyses. Yet, this method is widely used to visualize elemental distributions because it employs multiple detectors and can chemically (and sometimes isotopically) map up to seven elements. Although, NanoSIMS neither has the flexibility to easily analyze several volatile elements at the same time (detectors—i.e., electron multipliers and faraday cups—cannot be switched as easily as on a SIMS) nor the mass resolution power (MRP) to measure isotopic compositions of non-doped phases, its MRP and detection limits are sufficient to distinguish $^{12}C^-$, $^{14}N^{16}O^-$, and $^{32}S^-$ from interferences by neighboring mass peaks (Suer et al. 2017; Blanchard et al. 2022; Gao et al. 2022). Similar to SIMS analyses, C, N, and S abundances are determined from ^{12}C, $^{14}N^{16}O$, and ^{32}S, respectively, normalized to ^{29}Si or ^{28}Si (Fig. 11c, d); therefore, this method also requires reference materials with compositions/matrices similar to those of the experimental samples. Hydrogen contents, as H^-, can be quantified by NanoSIMS in experimental silicate glasses, but these analyses are more common for natural materials (e.g., Shilobreeva 2017).

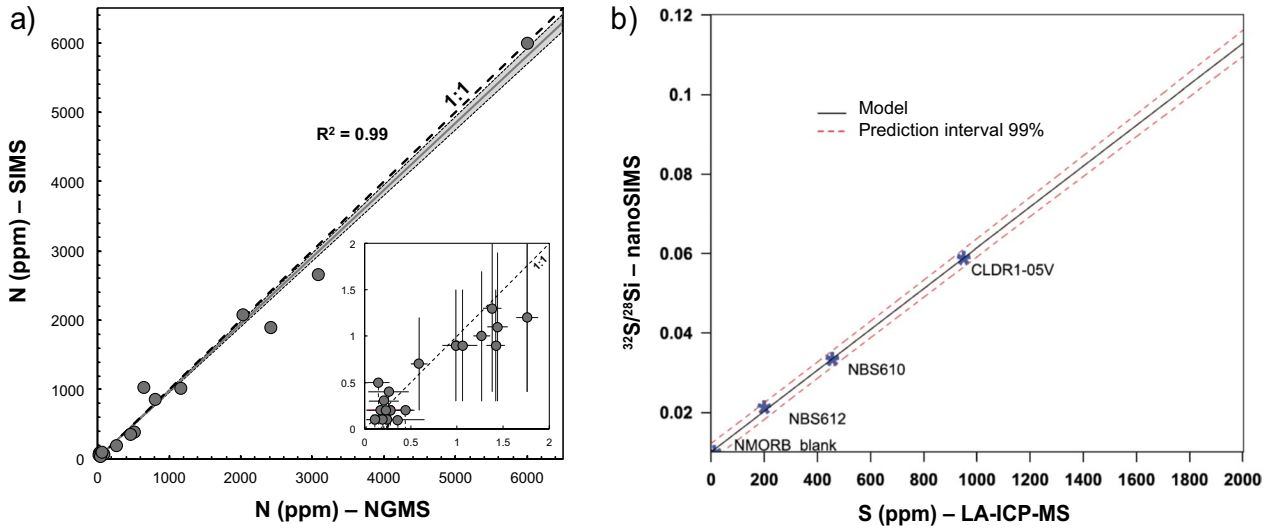

Fig. 10 **a** Comparison of N abundances measured by SIMS and NGMS in synthetic glasses (modified from Boulliung et al. 2020). (Inset) Low concentration data (< 2 ppm N) are shown on an enlarged scale. **b** NanoSIMS calibration curve for S analyses, with $^{32}S/^{28}Si$ determined by NanoSIMS reported as a function of S contents independently determined by laser ablation inductively coupled plasma mass spectrometry (LA-ICP-MS, modified from Suer et al. 2017)

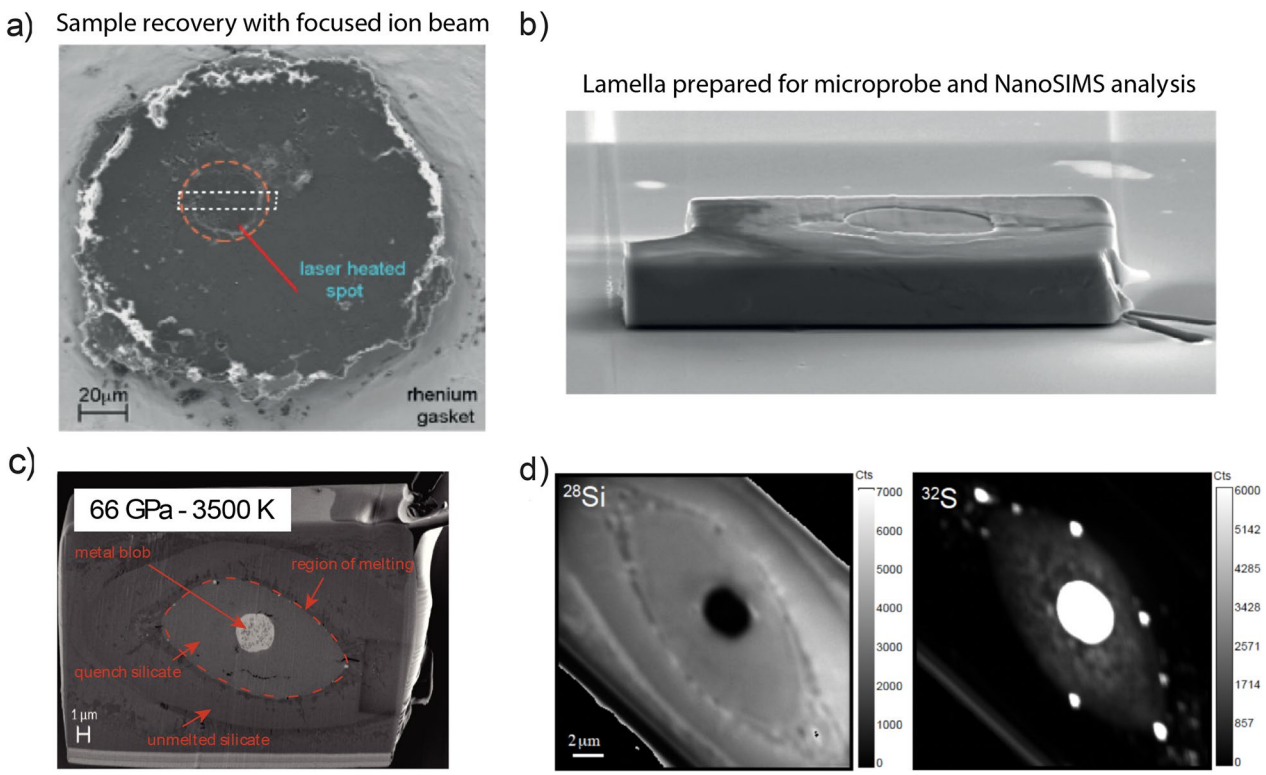

Fig. 11 LHDAC sample (modified from Suer et al. 2017) showing **a** and **b** LHDAC sample preparation for analysis, **c** a backscattered SEM image of a metal–silicate sample synthesized at 66 GPa and 3500 K, and **d** NanoSIMS chemical maps illustrating that most S is partitioned into the metal blob of that same sample, modified from Suer et al. (2017)

5.2.3 Laser ablation inductively coupled plasma mass spectrometry (LA-ICP-MS)

Sulfur contents in silicate and metallic phases can be also determined by LA-ICP-MS, although this technique is more destructive than SIMS (Table 1). Rather than a liquid introduction system found on a standard ICP-MS, the sample is directly ablated by a pulsed laser beam generally a few tens of μm in diameter. Therefore, this method is only adapted to LVP samples.

When the sample is fragmented to atomic levels within the ablation cell, a certain amount of matter is extracted from the surface of the sample by vaporization, generating aerosols of nanoparticles (a mixture of excited atoms, ions, molecules, and solid particles). The amount of material and the size of the particles removed depends on the nature of the sample analyzed and the energy of the laser, which can be regulated. To reduce thermal alteration of the sample, and thus lower the elemental fractionation during ablation, a flat-top-type homogeneous energy distribution and short-wavelength ultraviolet laser must be used. The aerosol is then transported by a helium gas flow to the plasma of the ICP-MS. The ions are electrostatically directed into a mass spectrometer, separated according to their mass-to-charge ratio, and eventually sent to a detector. As with SIMS or EPMA, quantitative analyses require calibration using external standard materials of known composition and with matrices similar to that of the analyzed sample. Few S concentrations determined by LA-ICP-MS have been reported in the literature because S measurements are challenging due to: (1) spectral interferences; (2) the lack of well-calibrated reference materials, particularly for silicates; and (3) problems with blank contamination, which become significant at low sulfur concentrations (Ripley et al. 2011). Yet, compared to SIMS analyses, the key feature of LA-ICP-MS is the ability to ablate a relatively large volume of material quickly, enabling a high signal-to-noise ratio.

With this method, sulfur contents have been determined in silicate glasses (Rottier and Audédat 2019) down to concentrations of 700 ppm. Rottier and Audédat (2019) tested the feasibility of S measurements by LA-ICP-MS in silicate glasses using a routine spot size of 40 μm, but also managed to analyze phases as small as 13 μm. Using a double correction method to account for a systematic drift between calculated and true sulfur concentrations, they quantified sulfur in silicate glasses down to several hundreds of parts per million; after correction, the difference between S concentrations obtained by EPMA and LA-ICP-MS was less than 5%.

5.2.4 Nuclear microprobe techniques

Hydrogen and carbon contents in experimental samples from metal–silicate equilibration experiments have been measured by nuclear microprobe techniques in LVP samples (e.g., Clesi et al. 2018; Malavergne et al. 2019). This technique is only suitable for LVP samples because of its low spatial resolution. In these methods, the interaction of an energetic ion beam with the target produces spectra from the reaction products (X-rays, charged particles). Hydrogen abundances in phases have been determined by elastic recoil detection analysis (ERDA; Bureau et al. 2009; Withers et al. 2012; Clesi et al. 2018), in which an incident $^{4}He^{+}$ beam is focused onto a large area (50×200 μm^2) of the polished sample and interacts with hydrogen. This interaction causes elastic recoil, ejecting the H nucleus from the sample surface for detection. ERDA does not require calibration (Bureau et al. 2009). As with SIMS, the analytical depth is limited to several micrometers beneath the surface. This method allows H determination at the micrometric scale with 5–15% relative uncertainties and a detection limit of 94 ppm H_2O (Bureau et al. 2009). Carbon abundances have been measured using nuclear reaction analysis (NRA), which employs a deuteron microbeam to produce the nuclear reaction $^{12}C(d,p)^{13}C$ upon interaction with the sample (Wang et al. 2010). The accuracy on such C determinations is 4–8% for metallic phases and 15–17% for silicate glasses (Malavergne et al. 2014).

Despite the numerous advantages of these methods, especially the fact that they are quasi absolute, spectral analyses require two-step processing using two distinct programs (RISMIN, Daudin et al. 2003; and SIMNRA, Mayer 1999) and perfect knowledge of the beam parameters and the major element compositions of the phases determined by EPMA. Sample preparation is not very different from that for SIMS volatile analyses: samples must be mirror-polished on one side, pressed into an indium mount, and stored both before and after gold coating in a furnace and/or desiccator to prevent volatile adsorption onto the sample surface. The main difference compared to SIMS mounts is that samples must be aligned across the mount because analyses are performed with a grazing angle of 75°.

5.2.5 Vibrational spectroscopy

IR and Raman spectroscopy are both vibrational techniques used to determine the speciation, and sometimes the abundances, of HVEs. IR spectroscopy is the result of light absorption by vibrating molecules, whereas the Raman effect is due to the scattering of light by the vibrating molecules. In both cases, the peak positions are determined by the vibrational energies associated with the bonds within the molecules of the sample. Hence, Raman and Fourier-transform IR (FTIR) spectra are often used and can be interpreted similarly. However, IR

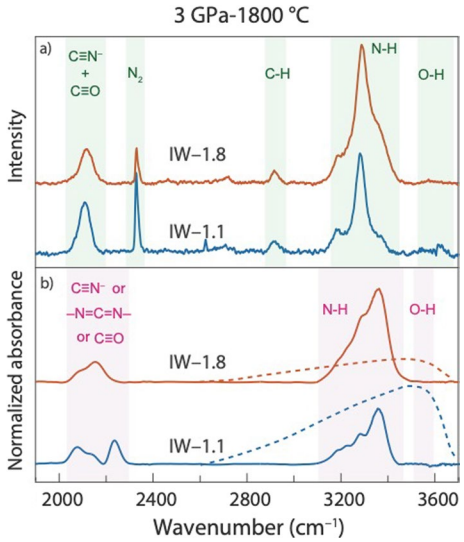

Fig. 12 Comparison of peaks associated with C–O–N–H species in **a** Raman spectra and **b** FTIR spectra of the same experimental silicate glasses produced at 3 GPa, 1800 °C, and IW–1.1 (blue) and IW–1.8 (orange) (modified from Grewal et al. 2020). **a** Background corrected Raman spectra, and **b** background corrected, thickness normalized FTIR spectra. The dashed curves show the broad asymmetric peak of O–H vibrations post-deconvolution from N–H stretching frequency in the similar range

is more sensitive to hetero-functional groups, i.e., polar functional groups such as molecules formed from H bonds, whereas Raman is more sensitive to homo-nuclear bonds such as O_2 or N_2. Therefore, polar bonds with high dipole moments such as NH_4^+ and H_2O are emphasized in FTIR spectra but appear very weak in Raman spectra. Conversely, highly polarizable bonds such as triple-bonded N_2, CN, O_2, or CO_2 are commonly emphasized in Raman spectra but appear very weak or inactive in FTIR spectra (Fig. 12). Nonetheless, the vibrations of numerous HVE-bearing molecules, particularly H-bonded molecules, are active in both IR and Raman spectra.

5.2.5.1 Infrared spectroscopy IR spectroscopy is one of the most popular methods for determining the abundance and speciation of the H-bearing moieties OH^- and molecular water in silicate phases because this technique is non-destructive, yet highly sensitive. Generally, the analyzed area can vary from a few square microns to 100×100 μm^2 depending on the HVE species and concentrations, as well as the sample's texture. Therefore, this method is only adapted to LVP samples. Analyses are most commonly performed in transmission mode, requiring that samples be transparent and doubly polished; this can present a challenge for small multiphase experimental samples. The sample thickness required generally varies from several hundreds of micrometers to < 10 μm, but depends on the HVE concentration. Therefore, doubly polished sections can be repeatedly measured and thinned to decrease a spectrum's signal-to-noise ratio and peak absorbances to less than 2 in both the near-infrared and mid-infrared regions (Mosenfelder et al. 2019). Notably, the measurement of the sample thickness often represents the largest source of error in transmission IR analyses.

The IR method is based on Beer's law:

$$A = \varepsilon \cdot c \cdot \ell, \tag{25}$$

where A is the absorbance, ε the molar absorption coefficient (M^{-1} cm^{-1}), c the molar concentration (M), and ℓ the optical path length (cm). This law describes the linear relationship between the number of infrared active bonds in a matrix and the quantity of absorption and allows the determination of the concentration of a species as $c = (W_M \cdot A)/(d \cdot \rho \cdot \varepsilon)$, where W_M is the molar weight (g/mol), d the sample thickness (equivalent toℓ), and ρ the density of the sample. Therefore, this method requires a specific calibration of the absorption coefficient,ε, for a given matrix composition and volatile species. Nonetheless, numerous studies of H in both natural and synthetic silicate glasses by IR analysis have demonstrated very good sensitivities and accuracies (down to a few ppm H; see review by Bureau et al. 2009).

5.2.5.2 Raman spectroscopy Because Raman spectroscopy employs visible wavelengths, it provides better spatial resolution (hundreds of nanometers to a few micrometers) than IR spectroscopy. Nevertheless, Raman spectroscopy has been essentially used for LVP samples (see references below).

Relatively recent studies determining H contents by micro-Raman spectroscopy (e.g., Mercier et al. 2009; Le Losq et al. 2012; Schiavi et al. 2018) have employed two methods called "external" and "internal" calibrations. "External" calibrations compare the intensity or integrated intensity of the water band (i.e., the height of the peak or the area under the peak, respectively) in an unknown sample to those of well-characterized standard glasses. Therefore, this method requires calibration curves as with SIMS, but in this case, the slopes of the curves must vary as a function of silicate glass composition. In contrast, "internal" calibrations normalize the intensity of the water band to those of bands in the silicate spectral region (e.g., Mercier et al. 2009; Le Losq et al. 2012), which tends to correct for or decrease the effects of instrumental and analytical conditions such as laser power fluctuations, focusing errors, and differences in confocal volume size, as well as differences in light absorption and reflectance that depend on the glass structure and composition. By combining these two calibration methods, Schiavi et al. (2018) improved

the accuracy of Raman H measurements to a relative standard deviation of ~ 4% (1σ) on average, though this reaches ~ 12% (1σ) for water contents of ~ 0.1 wt. %.

Although the detection limits are relatively high for some natural samples, both Raman and FTIR analyses are useful for experimental samples, which are usually enriched in H. The main advantages of Raman spectroscopy are that it requires minimal sample preparation (only a relatively flat surface), is non-destructive, and allows rapid analysis (within minutes) at high spatial resolution (Schiavi et al. 2018). Another advantage is that Raman signals can be gathered below the sample surface, which allowed Dalou et al. (2022) to determine C and N speciation in bubbles degassed from a reduced silicate melt analogous to a magma ocean.

Carbon can also be quantified by FTIR and micro-Raman spectroscopy with accuracies on the order of 0.2–0.4 wt.% (Amalberti et al. 2011, 2021; Morizet et al. 2013; Schanofski et al. 2023). However, all analytical developments for FTIR and Raman have focused on measuring C as CO_2 or CO_3^{2-} dissolved in silicate glasses. In reduced silicate glasses analogous to a magma ocean, C is dissolved as CH_4 or CN^-, or can even occur as graphite (Armstrong et al. 2015; Dalou et al. 2019b; Mosenfelder et al. 2019). Therefore, it is not yet possible to quantify the abundances of multiple C species in such reduced glasses (Armstrong et al. 2015), although their relative abundances can be investigated depending on P, T, fO_2, and composition (see Armstrong et al. 2015 for C; Dalou et al. 2019b and Mosenfelder et al. 2019 for N; Wilke et al. 2011 and Namur et al. 2016 for S).

6 Conclusions

The last two decades of advances in analytical methods have provided the experimental petrology community with methods for analyzing challenging, multiphase experimental samples comprising silicate glass, metal beads of various sizes, and bubbles. The achievement of DAC experiments coupled with the development of NanoSIMS has allowed laboratory simulations of conditions relevant to core formation and associated analyses. These very HP experiments have shown results in first-order agreement with results from experiments using large-volume apparatuses (Suer et al. 2023). Yet, partition coefficients obtained over a large range of temperature or pressure conditions show discrepancies that are not straightforward to understand (e.g., Rose-Weston et al. 2009; Suer et al. 2017, 2023). They may be related to changes in chemical behaviors across the large range of P–T conditions probed by large-volume apparatuses and DACs. Still, this implies partition coefficients should not be extrapolated beyond the P–T ranges in which they were measured (Suer et al. 2023).

Finally, whereas LVP studies show that oxygen fugacity is a key parameter controlling the solubility, and thus the degassing and metal–silicate partitioning, of HVEs (Suer et al. 2023), the specific effects of variable oxygen fugacities on metal–silicate partitioning of HVEs remains untested at > 25 GPa, i.e., in DAC experiments, due to technical challenges (e.g., Kulka 2021).

More generally, the complementary techniques reviewed herein have promoted large improvements in our understanding of the behaviors of HVEs during planetary formation processes. Nonetheless, an important gap remains: metallic reference materials are needed for the application of local analytical techniques such as SIMS or NanoSIMS to HVE analyses of metal blobs in experimental samples.

Acknowledgements
The authors thank Evelyn Füri and Laurette Piani for their support and fruitful discussions on analytical techniques. We are particularly grateful to Sumith Abeykoon and Pierre Condamine for providing unpublished figures and helping with references. We also thank Damanveer Grewal for providing original figures that helped make Fig. 12 and we warmly thank Robert Dennen for his English editing and his great help to improve Fig. 1, 5, 6 and 8. We are very grateful to two anonymous reviewers for their very helpful and constructive reviews and to associate editor Ohfuji san for managing our submission. This is CRPG contribution number 2856.

Author contributions
CD conceived, designed, and wrote the review. TAS wrote the LHDAC section and supervised the NanoSIMS section; LT wrote the low-pressure apparatuses sections, AG wrote the Mössbauer section, and WO wrote the XANES section, supervised by PS, who also contributed to the introduction, defining partitioning and solubility sections and the low-pressure apparatuses sections. All authors read and approved the final manuscript.

Funding
This work was supported by ANR CSI Planet.

Availability of data and materials
Not applicable.

Declarations

Competing interests
The authors declare no competing interests.

Received: 10 November 2023 Accepted: 23 April 2024
Published online: 07 May 2024

References

Amalberti J, Neuville DR, Sarda P, Sator N, Guillot B (2011) Quantification of CO_2 dissolved in silicate glasses and melts using Raman spectroscopy: implications for geodynamics. Mineral Mag 75:430

Amalberti J, Burnard P, Tissandier L, Laporte D (2018) The diffusion coefficients of noble gases (HeAr) in a synthetic basaltic liquid: one-dimensional diffusion experiments. Chem Geol 480:35–43

Amalberti J, Sarda P, Le Losq C, Sator N, Hammouda T, Chamorro-Pérez E, Neuville DR (2021) Raman spectroscopy to determine CO_2 solubility in mafic silicate melts at high pressure: haplobasaltic, haploandesitic and approach of basaltic compositions. Chem Geol 582:120413

Andrault D, Richet P, Piquet G, Gillet P, Itié JP, Haeusermann D, Hanfland M (1998) Thermal pressure in the laser-heated diamond-anvil cell: an X-ray diffraction study. Eur J Mineral 10:931–940
Andrault D, Bolfan-Casanova N, Ohtaka O, Fukui H, Arima H, Fialin M, Funakoshi K (2009) Melting diagrams of Fe-rich alloys determined from synchrotron in situ measurements in the 15–23 GPa pressure range. Phys Earth Planet Inter 174(1–4):181–191
Anzellini S, Boccato S (2020) A practical review of the laser-heated diamond anvil cell for university laboratories and synchrotron applications. Crystals 10(6):459
Ardia P, Hirschmann MM, Withers AC, Stanley BD (2013) Solubility of CH4 in a synthetic basaltic melt, with applications to atmosphere–magma ocean–core partitioning of volatiles and to the evolution of the Martian atmosphere. Geochim Cosmochim Acta 114:52–71
Armstrong LS, Hirschmann MM, Stanley BD, Falksen EG, Jacobsen SD (2015) Speciation and solubility of reduced C–O–H–N volatiles in mafic melt: implications for volcanism, atmospheric evolution, and deep volatile cycles in the terrestrial planets. Geochim Cosmochim Acta 171:283–302
Aukrust E, Muan A (1962) Thermodynamic properties of Pd- Fe alloys in the temperature range 1200–1460 °C. Acta Metall 10(5):555–560
Auzende AL, Gillot J, Coquet A, Hennet L, Ona-Nguema G, Bonnin D, Fiquet G (2011) Synthesis of amorphous MgO-rich peridotitic starting material for laser-heated diamond anvil cell experiments–application to iron partitioning in the mantle. High Press Res 31(1):199–213
Badro J, Sossi PA, Deng Z, Borensztajn S, Wehr N, Ryerson FJ (2021) Experimental investigation of elemental and isotopic evaporation processes by laser heating in an aerodynamic levitation furnace. C R Géosci 353(1):101–114
Badwal SPS, Bannister MJ, Garrett WG (1987) Oxygen measurement with SIRO2 sensors. J Phys E: Sci Instrum 20(5):531
Bajt S, Sutton SR, Delaney JS (1994) X-ray microprobe analysis of iron oxidation states in silicates and oxides using X-ray absorption near edge structure (XANES). Geochim Cosmochim Acta 58(23):5209–5214
Ballhaus C, Fonseca RO, Münker C, Rohrbach A, Nagel T, Speelmanns IM, Heuser A (2017) The great sulfur depletion of Earth's mantle is not a signature of mantle–core equilibration. Contrib Mineral Petrol 172:1–10
Bancroft GM, Maddock AG, Burns RG (1967) Applications of the Mössbauer effect to silicate mineralogy—I. Iron silicates of known crystal structure. Geochim Cosmochim Acta 31:2219–2246
Benedetti LR, Loubeyre P (2004) Temperature gradients, wavelength-dependent emissivity, and accuracy of high and very-high temperatures measured in the laser-heated diamond cell. High Press Res 24(4):423–445
Bernadou F, Gaillard F, Füri E, Marrocchi Y, Slodczyk A (2021) Nitrogen solubility in basaltic silicate melt-Implications for degassing processes. Chem Geol 573:120192
Berry AJ, O'Neill HSC (2004) A XANES determination of the oxidation state of chromium in silicate glasses. Am Mineral 89:790–798
Berry AJ, O'Neill HSC, Jayasuriya KD, Campbell SJ, Foran GJ (2003) XANES calibrations for the oxidation state of iron in a silicate glass. Am Mineral 88:967–977
Berry AJ, Hack AC, Mavrogenes JA, Newville M, Sutton SR (2006) A XANES study of Cu speciation in high-temperature brines using synthetic fluid inclusions. Am Mineral 91:1773–1782
Berry AJ, Yaxley GM, Woodland AB, Foran GJ (2010) A XANES calibration for determining the oxidation state of iron in mantle garnet. Chem Geol 278(1–2):31–37
Berry AJ, Stewart GA, O'Neill HSC, Mallmann G, Mosselmans JFW (2018) A re-assessment of the oxidation state of iron in MORB glasses. Earth Planet Sci Lett 483:114–123
Blanchard I, Rubie DC, Jennings ES, Franchi IA, Zhao X, Petitgirard S, Morbidelli A (2022) The metal–silicate partitioning of carbon during Earth's accretion and its distribution in the early solar system. Earth Planet Sci Lett 580:117374
Boehler R (2000) High-pressure experiments and the phase diagram of lower mantle and core materials. Rev Geophys 38(2):221–245
Bondar D, Fei H, Withers AC, Ishii T, Chanyshev A, Katsura T (2021) A simplified rapid-quench multi-anvil technique. Rev Sci Instrum 92(11):113902
Borisov AA (2008) Experimental investigation of K and Na partitioning between miscible liquids. Petrology 16:552–564
Bouhifd MA, Jephcoat AP (2011) Convergence of Ni and Co metal–silicate partition coefficients in the deep magma-ocean and coupled silicon–oxygen solubility in iron melts at high pressures. Earth Planet Sci Lett 307(3–4):341–348
Boujibar A, Andrault D, Bouhifd MA, Bolfan-Casanova N, Devidal JL, Trcera N (2014) Metal–silicate partitioning of sulphur, new experimental and thermodynamic constraints on planetary accretion. Earth Planet Sci Lett 391:42–54
Boulliung J, Wood BJ (2022) SO_2 solubility and degassing behavior in silicate melts. Geochim Cosmochim Acta 336:150–164
Boulliung J, Füri E, Dalou C, Tissandier L, Zimmermann L, Marrocchi Y (2020) Oxygen fugacity and melt composition controls on nitrogen solubility in silicate melts. Geochim Cosmochim Acta 284:120–133
Boulliung J, Dalou C, Tissandier L, Füri E, Marrocchi Y (2021) Nitrogen diffusion in silicate melts under reducing conditions. Am Miner 106(4):662–666
Bower DJ, Hakim K, Sossi PA, Sanan P (2022) Retention of water in terrestrial magma oceans and carbon-rich early atmospheres. Planet Sci J 3(4):93
Brounce M, Boyce J, McCubbin FM, Humphreys J, Reppart J, Stolper E, Eiler J (2019) The oxidation state of sulfur in lunar apatite. Am Miner 104(2):307–312
Bureau H, Raepsaet C, Khodja H, Carraro A, Aubaud C (2009) Determination of hydrogen content in geological samples using elastic recoil detection analysis (ERDA). Geochim Cosmochim Acta 73(11):3311–3322
Burkemper LK, Agee CB, Garcia KA (2012) Constraints on core formation from molybdenum solubility in silicate melts at high pressure. Earth Planet Sci Lett 335:95–104
Burnham AD, Berry AJ, Halse HR, Schofield PF, Cibin G, Mosselmans JFW (2015) The oxidation state of europium in silicate melts as a function of oxygen fugacity, composition and temperature. Chem Geol 411:248–259
Burns RG, Solberg TC (1990) ^{57}Fe-bearing oxide, silicate, and aluminosilicate minerals, in: spectroscopic characterization of minerals and their surfaces. ACS Symposium Series. American Chemical Society, pp 262–283
Campbell AJ (2008) Measurement of temperature distributions across laser heated samples by multispectral imaging radiometry. Rev Sci Instrum 79(1):015108
Cartier C, Wood BJ (2019) The role of reducing conditions in building Mercury. Elem: Int Mag Mineral Geochem Petrol 15(1):39–45
Cartier C, Hammouda T, Boyet M, Bouhifd MA, Devidal JL (2014) Redox control of the fractionation of niobium and tantalum during planetary accretion and core formation. Nat Geosci 7(8):573–576
Cartier C, Llado L, Pirotte H, Tissandier L, Namur O, Charlier B, Collinet M (2023). i and Co metal/silicate partitioning: tracing pressure and oxygen fugacity conditions of planetary differentiation. In: Goldschmidt 2023 conference
Charnoz S, Sossi PA, Lee YN, Siebert J, Hyodo R, Allibert L, Moynier F (2021) Tidal pull of the Earth strips the proto-Moon of its volatiles. Icarus 364:114451
Chase MW, National Information Standards Organization (US) (1998) NIST-JANAF thermochemical tables, vol 9. American Chemical Society, Washington, DC, pp 1–1951
Chevreux P, Tissandier L, Laplace A, Vitova T, Bahl S, Le Guyadec F, Deloule E (2021) Uranium solubility and speciation in reductive soda-lime aluminosilicate glass melts. J Nucl Mater 544:152666
Chi H, Dasgupta R, Duncan MS, Shimizu N (2014) Partitioning of carbon between Fe-rich alloy melt and silicate melt in a magma ocean–implications for the abundance and origin of volatiles in Earth, Mars, and the Moon. Geochim Cosmochim Acta 139:447–471
Chidester BA, Lock SJ, Swadba KE, Rahman Z, Righter K, Campbell AJ (2022) The lithophile element budget of Earth's core. Geochem Geophys Geosyst 23(2):e2021GC009986
Choy JH, Jung H, Yoon JB (2001) Co K-edge XAS study on a new cobalt-doped-SiO_2 pillared clay. J Synchrotron Radiat 8:599–601
Cicconi MR, Neuville DR, Tannou I, Baudelet F, Floury P, Paris E, Giuli G (2015) Letter. Competition between two redox states in silicate melts: an in-situ experiment at the Fe K-edge and Eu L3-edge. Am Mineral 100(4):1013–1016
Clesi V, Bouhifd MA, Bolfan-Casanova N, Manthilake G, Schiavi F, Raepsaet C, Andrault D (2018) Low hydrogen contents in the cores of terrestrial planets. Sci Adv 4(3):e1701876

Condamine P, Tournier S, Charlier B, Médard E, Triantafyllou A, Dalou C, Marrocchi Y (2022) Influence of intensive parameters and assemblies on friction evolution during piston-cylinder experiments. Am Mineral: J Earth Planet Mater 107(8):1575–1581

Corgne A, Keshav S, Wood BJ, McDonough WF, Fei Y (2008) Metal–silicate partitioning and constraints on core composition and oxygen fugacity during Earth accretion. Geochim Cosmochim Acta 72(2):574–589

Cormier L, Dargaud O, Menguy N, Henderson GS, Guignard M, Trcera N, Watts B (2011) Investigation of the role of nucleating agents in MgO-SiO_2-Al_2O_3-SiO_2-TiO_2 glasses and glass-ceramics: a XANES study at the Ti K- and L2,3-edges. Cryst Growth Des 11:311–319

Corrigan G, Gibb FG (1979) The loss of Fe and Na from a basaltic melt during experiments using the wire-loop method. Mineral Mag 43(325):121–126

Cottrell E, Gardner JE, Rutherford MJ (1999) Petrologic and experimental evidence for the movement and heating of the pre-eruptive Minoan rhyodacite (Santorini, Greece). Contrib Miner Petrol 135(4):315–331

Cottrell E, Walter MJ, Walker D (2009) Metal–silicate partitioning of tungsten at high pressure and temperature: implications for equilibrium core formation in Earth. Earth Planet Sci Lett 281(3–4):275–287

Dalou C, Hirschmann MM, von der Handt A, Mosenfelder J, Armstrong LS (2017) Nitrogen and carbon fractionation during core–mantle differentiation at shallow depth. Earth Planet Sci Lett 458:141–151

Dalou C, Füri E, Deligny C, Piani L, Caumon MC, Laumonier M, Edén M (2019a) Redox control on nitrogen isotope fractionation during planetary core formation. Proc Natl Acad Sci 116(29):14485–14494

Dalou C, Hirschmann MM, Jacobsen SD, Le Losq C (2019b) Raman spectroscopy study of COHN speciation in reduced basaltic glasses: implications for reduced planetary mantles. Geochim Cosmochim Acta 265:32–47

Dalou C, Deligny C, Füri E (2022) Nitrogen isotope fractionation during magma ocean degassing: tracing the composition of early Earth's atmosphere. Geochem Perspect Lett 20:27–31

Dasgupta R, Chi H, Shimizu N, Buono AS, Walker D (2013) Carbon solution and partitioning between metallic and silicate melts in a shallow magma ocean: implications for the origin and distribution of terrestrial carbon. Geochim Cosmochim Acta 102:191–212

Daudin L, Khodja H, Gallien JP (2003) Development of "position–charge–time" tagged spectrometry for ion beam microanalysis. Nucl Instrum Methods Phys Res, Sect B 210:153–158

De Grave E, Van Alboom A (1991) Evaluation of ferrous and ferric Mössbauer fractions. Phys Chem Miner 18:337–342

Dehant V, Lammer H, Kulikov YN, Grießmeier JM, Breuer D, Verhoeven O, Lognonné P (2007) Planetary magnetic dynamo effect on atmospheric protection of early Earth and Mars. Space Sci Rev 129:279–300

Delaney JR, Karsten JL (1981) Ion microprobe studies of water in silicate melts. Concentration-dependent water diffusion in obsidian. Earth Planet Sci Lett 52(1):191–202

Deloule É, Paillat O, Pichavant M, Scaillet B (1995) Ion microprobe determination of water in silicate glasses: methods and applications. Chem Geol 125(1–2):19–28

Deng J, Du Z, Benedetti LR, Lee KK (2017) The influence of wavelength-dependent absorption and temperature gradients on temperature determination in laser-heated diamond-anvil cells. J Appl Phys 121(2):025901

Desai PD (1986) Thermodynamic properties of iron and silicon. J Phys Chem Ref Data 15(3):967–983

Dewaele A, Loubeyre P, Mezouar M (2004) Equations of state of six metals above 94 GPa. Phys Rev B 70(9):094112

Donaldson CH (1979) Composition changes in a basalt melt contained in a wire loop of Pt80Rh20; effects of temperature, time, and oxygen fugacity. Mineral Mag 43:115–119

Donaldson CH, Williams RJ, Lofgren G (1975) A sample holding technique for study of crystal growth in silicate melts. Am Mineral: J Earth Planet Mater 60(3–4):324–326

Du Z, Amulele G, Robin Benedetti L, Lee KK (2013) Mapping temperatures and temperature gradients during flash heating in a diamond-anvil cell. Rev Sci Instrum 84(7):075111

Dunn T, Luth RW (1993) The piston-cylinder apparatus. Mineralogical Association of Canada, Short Course Handbook, vol 21, pp 39–94

Dyar MD, Agresti DG, Schaefer MW, Grant CA, Sklute EC (2006) Mössbauer spectroscopy of earth and planetary materials. Annu Rev Earth Planet Sci 34:83–125

Dyar MD, McCanta M, Breves E, Carey CJ, Lanzirotti A (2016) Accurate predictions of iron redox state in silicate glasses: a multivariate approach using X-ray absorption spectroscopy. Am Miner 101(3):744–747

Eggert JH, Goettel KA, Silvera IF (1989) Ruby at high pressure. I. Optical line shifts to 156 GPa. Phys Rev B 40(8):5724

Elkins-Tanton LT (2008) Linked magma ocean solidification and atmospheric growth for Earth and Mars. Earth Planet Sci Lett 271(1–4):181–191

Eremets MI, Minkov VS, Kong PP, Drozdov AP, Chariton S, Prakapenka VB (2023) Universal diamond edge Raman scale to 0.5 terapascal and implications for the metallization of hydrogen. Nat Commun 14(1):907

Essilfie-Dughan J, Hendry MJ, Warner J, Kotzer T (2012) Microscale mineralogical characterization of As, Fe, and Ni in uranium mine tailings. Geochim Cosmochim Acta 96:336–352

Ezad IS, Shcheka SS, Buhre S, Buhre A, Gorojovsky LR, Shea JJ, Foley SF (2023) Rapid quench piston cylinder apparatus: an improved design for the recovery of volatile-rich geological glasses from experiments at 0.5–2.5 GPa. Rev Sci Instrum 94(5):055107

Ferreira PG, de Ligny D, Lazzari O, Jean A, Gonzalez OC, Neuville DR (2013) Photoreduction of iron by a synchrotron X-ray beam in low iron content soda-lime silicate glasses. Chem Geol 346:106–112

Fichtner CE, Schmidt MW, Liebske C, Bouvier AS, Baumgartner LP (2021) Carbon partitioning between metal and silicate melts during Earth accretion. Earth Planet Sci Lett 554:116659

Fiege A, Ruprecht P, Simon AC, Bell AS, Göttlicher J, Newville M, Lanzirotti T, Moore G (2017) Calibration of Fe XANES for high-precision determination of Fe oxidation state in glasses: Comparison of new and existing results obtained at different synchrotron radiation sources. Am Miner 102(2):369–380

Fiquet G, Auzende AL, Siebert J, Corgne A, Bureau H, Ozawa H, Garbarino G (2010) Melting of peridotite to 140 gigapascals. Science 329(5998):1516–1518

Fischer RA, Nakajima Y, Campbell AJ, Frost DJ, Harries D, Langenhorst F, Rubie DC (2015) High pressure metal–silicate partitioning of Ni Co, V, Cr, Si, and O. Geochim Cosmochim Acta 167:177–194

Fischer RA, Cottrell E, Hauri E, Lee KK, Le Voyer M (2020) The carbon content of Earth and its core. Proc Natl Acad Sci 117(16):8743–8749

Foley BJ, Driscoll PE (2016) Whole planet coupling between climate, mantle, and core: implications for rocky planet evolution. Geochem Geophys Geosyst 17(5):1885–1914

Füri E, Deloule E, Dalou C (2018) Nitrogen abundance and isotope analysis of silicate glasses by secondary ionization mass spectrometry. Chem Geol 493:327–337

Gaborieau M, Laubier M, Bolfan-Casanova N, McCammon CA, Vantelon D, Chumakov AI, Schiavi F, Neuville DR, Venugopal S (2020) Determination of Fe3+/ΣFe of olivine-hosted melt inclusions using Mössbauer and XANES spectroscopy. Chem Geol 547:119646

Gaetani GA, Grove TL (1997) Partitioning of moderately siderophile elements among olivine, silicate melt, and sulfide melt: Constraints on core formation in the Earth and Mars. Geochim Cosmochim Acta 61(9):1829–1846

Gaillard F, Schmidt B, Mackwell S, McCammon C (2003) Rate of hydrogen–iron redox exchange in silicate melts and glasses. Geochim Cosmochim Acta 67(13):2427–2441

Galoisy L, Calas G, Arrio MA (2001) High-resolution XANES spectra of iron in minerals and glasses: structural information from the pre-edge region. Chem Geol 174:307–319

Gao Z, Yang YN, Yang SY, Li Y (2022) Experimental determination of N2 solubility in silicate melts and implications for N2–Ar–CO2 fractionation in magmas. Geochim Cosmochim Acta 326:17–40

Gardner JE, Hilton M, Carroll MR (1999) Experimental constraints on degassing of magma: isothermal bubble growth during continuous decompression from high pressure. Earth Planet Sci Lett 168(1–2):201–218

Georges P, Libourel G, Deloule E (2000) Experimental constraints on alkali condensation in chondrule formation. Meteorit Planet Sci 35(6):1183–1188

Grewal DS, Dasgupta R, Holmes AK, Costin G, Li Y, Tsuno K (2019) The fate of nitrogen during core-mantle separation on Earth. Geochim Cosmochim Acta 251:87–115
Grewal DS, Dasgupta R, Farnell A (2020) The speciation of carbon, nitrogen, and water in magma oceans and its effect on volatile partitioning between major reservoirs of the Solar System rocky bodies. Geochim Cosmochim Acta 280:281–301
Grewal DS, Dasgupta R, Hough T, Farnell A (2021) Rates of protoplanetary accretion and differentiation set nitrogen budget of rocky planets. Nat Geosci 14(6):369–376
Grewal DS, Sun T, Aithala S, Hough T, Dasgupta R, Yeung LY, Schauble EA (2022) Limited nitrogen isotopic fractionation during core-mantle differentiation in rocky protoplanets and planets. Geochim Cosmochim Acta 338:347–364
Grove TL (1982) Use of FePt alloys to eliminate the iron loss problem in 1 atmosphere gas mixing experiments: theoretical and practical considerations. Contrib Miner Petrol 78(3):298–304
Gütlich P, Link R, Trautwein AX (1978) Mössbauer spectroscopy and transition metal chemistry, inorganic chemistry concepts. Springer, Berlin
Hamilton DL, Burnham CW, Osborn EF (1964) The solubility of water and effects of oxygen fugacity and water content on crystallization in mafic magmas. J Petrol 5(1):21–39
Hauri E (2002) SIMS analysis of volatiles in silicate glasses, 2: isotopes and abundances in Hawaiian melt inclusions. Chem Geol 183(1–4):115–141
Hauri E, Wang J, Dixon JE, King PL, Mandeville C, Newman S (2002) SIMS analysis of volatiles in silicate glasses: 1. Calibration, matrix effects and comparisons with FTIR. Chem Geol 183(1–4):99–114
Hawthorne FC, Waychunas GA (1988) Spectrum fitting methods. Rev Mineral 18:63–98
Heinz DL, Jeanloz R (1987) Temperature measurements in the laser-heated diamond cell. High-pressure research in mineral physics: a volume in honor of Syun-iti Akimoto, vol 39, pp 113–127
Henderson GS, De Groot FMF, Moulton BJA (2014) X-ray absorption near-edge structure (XANES) spectroscopy. Rev Mineral Geochem 78:75–138
Hennet L, Pozdnyakova I, Bytchkov A, Cristiglio V, Palleau P, Fischer HE, Cuello GJ, Johnson M, Melin P, Zanghi D, Brassamin S (2006) Levitation apparatus for neutron diffraction investigations on high temperature liquids. Rev Sci Instrum 77(5):053903
Hervig RL (1992) Ion probe microanalyses for volatile elements in melt inclusions (abst.). EOS Trans Am Geophys Union 73:367
Hirschmann MM (2012) Magma ocean influence on early atmosphere mass and composition. Earth Planet Sci Lett 341:48–57
Hirschmann MM, Withers AC, Ardia P, Foley NT (2012) Solubility of molecular hydrogen in silicate melts and consequences for volatile evolution of terrestrial planets. Earth Planet Sci Lett 345:38–48
Holloway JR, Dixon JE, Pawley AR (1992) An internally heated, rapid-quench, high-pressure vessel. Am Miner 77(5–6):643–646
Holzheid A, Palme H, Chakraborty S (1997) The activities of NiO, CoO and FeO in silicate melts. Chem Geol 139(1–4):21–38
Iizuka-Oku R, Yagi T, Gotou H, Okuchi T, Hattori T, Sano-Furukawa A (2017) Hydrogenation of iron in the early stage of Earth's evolution. Nat Commun 8(1):14096
Ishii T, Yamazaki D, Tsujino N, Xu F, Liu Z, Kawazoe T, Katsura T (2017) Pressure generation to 65 GPa in a Kawai-type multi-anvil apparatus with tungsten carbide anvils. High Press Res 37(4):507–515
Ishii T, Miyajima N, Criniti G, Hu Q, Glazyrin K, Katsura T (2022) High pressure-temperature phase relations of basaltic crust up to mid-mantle conditions. Earth Planet Sci Lett 584:117472
Ishii T, Frost DJ, Kim EJ, Chanyshev A, Nishida K, Wang B, Katsura T (2023) Buoyancy of slabs and plumes enhanced by curved post-garnet phase boundary. Nat Geosci 16(9):828–832
Jackson CRM, Cottrell E, Du Z, Bennett NR, Fei Y (2021) High pressure redistribution of nitrogen and sulfur during planetary stratification. Geochem Perspect Lett 18:37–42
Jahn S, Kowalski PM (2014) Theoretical approaches to structure and spectroscopy of earth materials. Rev Mineral Geochem 78:691–743
Jayasuriya KD, O'Neill HSC, Berry AJ, Campbell SJ (2004) A Mossbauer study of the oxidation state of Fe in silicate melts. Am Miner 89(11–12):1597–1609
Jennings ES (2020) Using complementary microanalytical techniques to analyse diamond anvil cell experiments. In: IOP conference series: materials science and engineering, vol 891, no 1. IOP Publishing, p. 012015
Kasting JF, Siefert JL (2002) Life and the evolution of Earth's atmosphere. Science 296(5570):1066–1068
Khedim H, Podor R, Rapin C, Vilasi M (2008) Redox-control solubility of chromium oxide in soda-silicate melts. J Am Ceram Soc 91(11):3571–3579
Kilburn MR, Wood BJ (1997) Metal–silicate partitioning and the incompatibility of S and Si during core formation. Earth Planet Sci Lett 152(1–4):139–148
Kleine T, Rudge JF (2011) Chronometry of meteorites and the formation of the Earth and Moon. Elements 7(1):41–46
Knibbe JS, Luginbühl SM, Stoevelaar R, van der Plas W, van Harlingen DM, Rai N, van Westrenen W (2018) Calibration of a multi-anvil high-pressure apparatus to simulate planetary interior conditions. EPJ Tech Instrum 5:1–14
Kulka BL (2021) Possible control of redox conditions in the laser-heated diamond anvil cell. Doctoral dissertation, Arizona State University
Kunimoto T, Irifune T, Tange Y, Wada K (2016) Pressure generation to 50 GPa in Kawai-type multianvil apparatus using newly developed tungsten carbide anvils. High Press Res 36(2):97–104
Kuwahara H, Kagoshima T, Nakada R, Ogawa N, Yamaguchi A, Sano Y, Irifune T (2019a) Fluorine and chlorine fractionation during magma ocean crystallization: constraints on the origin of the non-chondritic F/Cl ratio of the Earth. Earth Planet Sci Lett 520:241–249
Kuwahara H, Itoh S, Nakada R, Irifune T (2019b) The effects of carbon concentration and silicate composition on the metal-silicate partitioning of carbon in a shallow magma ocean. Geophys Res Lett 46(16):9422–9429
Labidi J, Shahar A, Le Losq C, Hillgren VJ, Mysen BO, Farquhar J (2016) Experimentally determined sulfur isotope fractionation between metal and silicate and implications for planetary differentiation. Geochim Cosmochim Acta 175:181–194
Landron C, Hennet L, Coutures JP, Jenkins T, Alétru C, Greaves N, Derbyshire G (2000) Aerodynamic laser-heated contactless furnace for neutron scattering experiments at elevated temperatures. Rev Sci Instrum 71(4):1745–1751
Le Losq C, Neuville DR, Moretti R, Roux J (2012) Amorphous materials: determination of water content in silicate glasses using Raman spectrometry: implications for the study of explosive volcanism. Am Miner 97(5–6):779–790
Lerner AH, Muth MJ, Wallace PJ, Lanzirotti A, Newville M, Gaetani GA, Chowdhury P, Dasgupta R (2021) Improving the reliability of Fe-and S-XANES measurements in silicate glasses: correcting beam damage and identifying Fe-oxide nanolites in hydrous and anhydrous melt inclusions. Chem Geol 586:120610
Li Y, Dasgupta R, Tsuno K (2015) The effects of sulfur, silicon, water, and oxygen fugacity on carbon solubility and partitioning in Fe-rich alloy and silicate melt systems at 3 GPa and 1600 C: implications for core–mantle differentiation and degassing of magma oceans and reduced planetary mantles. Earth Planet Sci Lett 415:54–66
Li YF, Marty B, Shcheka S, Zimmermann L, Keppler H (2016) Nitrogen isotope fractionation during terrestrial core-mantle separation. Geochem Perspect Lett 2:138–147
Li Y, Wiedenbeck M, Monteleone B, Dasgupta R, Costin G, Gao Z, Lu W (2023) Nitrogen and carbon fractionation in planetary magma oceans and origin of the superchondritic C/N ratio in the bulk silicate Earth. Earth Planet Sci Lett 605:118032
Libourel G, Marty B, Humbert F (2003) Nitrogen solubility in basaltic melt. Part I. Effect of oxygen fugacity. Geochim Cosmochim Acta 67(21):4123–4135
Lin JF, Shu J, Mao HK, Hemley RJ, Shen G (2003) Amorphous boron gasket in diamond anvil cell research. Rev Sci Instrum 74(11):4732–4736
Lobanov SS, Speziale S, Lin JF, Schifferle L, Schreiber A (2021) Radiometric temperature determination in nongray bridgmanite: applications to melting curve and post-perovskite transition boundary in the lower mantle. J Geophys Res: Solid Earth 126(5):e2021JB021723
Lord OT, Wann ET, Hunt SA, Walker AM, Santangeli J, Walter MJ, Mezouar M (2014) The NiSi melting curve to 70 GPa. Phys Earth Planet Inter 233:13–23

Ma Z (2001) Thermodynamic description for concentrated metallic solutions using interaction parameters. Metall Mater Trans B 32:87–103
Mahan B, Siebert J, Blanchard I, Badro J, Kubik E, Sossi P, Moynier F (2018) Investigating Earth's formation history through copper and sulfur metal-silicate partitioning during core-mantle differentiation. J Geophys Res: Solid Earth 123(10):8349–8363
Malavergne V, Cordier P, Righter K, Brunet F, Zanda B, Addad A, Hewins RH (2014) How Mercury can be the most reduced terrestrial planet and still store iron in its mantle. Earth Planet Sci Lett 394:186–197
Malavergne V, Bureau H, Raepsaet C, Gaillard F, Poncet M, Surble S, Khodja H (2019) Experimental constraints on the fate of H and C during planetary core-mantle differentiation. Implications for the Earth. Icarus 321:473–485
Mao HK, Bell PM, Shaner JW, Steinberg DJ (1978) Specific volume measurements of Cu, Mo, Pd, and Ag and calibration of the ruby R 1 fluorescence pressure gauge from 0.06 to 1 Mbar'. J Appl Phys 49:3276–3283
Mathieu R, Khedim H, Libourel G, Podor R, Tissandier L, Deloule E, Vilasi M (2008) Control of alkali-metal oxide activity in molten silicates. J Non-Cryst Solids 354(45–46):5079–5083
Mathieu R, Libourel G, Deloule E, Tissandier L, Rapin C, Podor R (2011) Na_2O solubility in CaO–MgO–SiO_2 melts. Geochim Cosmochim Acta 75(2):608–628
Mayer M (1999) SIMNRA, a simulation program for the analysis of NRA, RBS and ERDA. In: AIP conference proceedings, vol 475, no 1. American Institute of Physics, pp 541–544
McCammon CA (2000) Insights into phase transformations from Mössbauer spectroscopy. Rev Mineral Geochem 39(1):241–264
McCammon CA (2003) Mössbauer spectroscopy in the geosciences: highlights and perspectives. In: Gütlich P, Fitzsimmons BW, Rüffer R, Spiering H (eds) Mössbauer spectroscopy. Springer, Dordrecht, pp 289–296
McCammon C (2021) Mössbauer spectroscopy with high spatial resolution: spotlight on geoscience. In: Yoshida Y, Langouche G (eds) Modern Mössbauer spectroscopy: new challenges based on cutting-edge techniques, topics in applied physics. Springer, Singapore, pp 221–266
McCammon C, Kopylova MG (2004) A redox profile of the Slave mantle and oxygen fugacity control in the cratonic mantle. Contrib Miner Petrol 148:55–68
Médard E, McCammon CA, Barr JA, Grove TL (2008) Oxygen fugacity, temperature reproducibility, and H_2O contents of nominally anhydrous piston-cylinder experiments using graphite capsules. Am Miner 93(11–12):1838–1844
Mendybaev RA, Beckett JR, Stolper E, Grossman L (1998) Measurement of oxygen fugacities under reducing conditions: Non-Nernstian behavior of Y_2O_3-doped zirconia oxygen sensors. Geochim Cosmochim Acta 62(18):3131–3139
Mercier M, Di Muro A, Giordano D, Métrich N, Lesne P, Pichavant M, Montagnac G (2009) Influence of glass polymerisation and oxidation on micro-Raman water analysis in alumino-silicate glasses. Geochim Cosmochim Acta 73(1):197–217
Merkel S, Yagi T (2005) X-ray transparent gasket for diamond anvil cell high pressure experiments. Rev Sci Instrum 76(4):046109
Métrich N, Berry AJ, O'Neill HSC, Susini J (2009) The oxidation state of sulfur in synthetic and natural glasses determined by X-ray absorption spectroscopy. Geochim Cosmochim Acta 73(8):2382–2399
Moore G, Carmichael ISE (1998) The hydrous phase equilibria (to 3 kbar) of an andesite and basaltic andesite from western Mexico: constraints on water content and conditions of phenocryst growth. Contrib Miner Petrol 130(3):304–319
Morizet Y, Brooker RA, Iacono-Marziano G, Kjarsgaard BA (2013) Quantification of dissolved CO2 in silicate glasses using micro-Raman spectroscopy. Am Miner 98(10):1788–1802
Mosenfelder JL, von der Handt A, Füri E, Dalou C, Hervig RL, Rossman GR, Hirschmann MM (2019) Nitrogen incorporation in silicates and metals: results from SIMS, EPMA, FTIR, and laser-extraction mass spectrometry. Am Mineral: J Earth Planet Mater 104(1):31–46
Mössbauer RL (1958) Kernresonanzfluoreszenz von Gammastrahlung in Ir191. Z Phys 151:124–143
Namur O, Charlier B, Holtz F, Cartier C, McCammon C (2016) Sulfur solubility in reduced mafic silicate melts: implications for the speciation and distribution of sulfur on Mercury. Earth Planet Sci Lett 448:102–114
Nash WM, Smythe DJ, Wood BJ (2019) Compositional and temperature effects on sulfur speciation and solubility in silicate melts. Earth Planet Sci Lett 507:187–198
Neuville DR, Hennet L, Florian P, de Ligny D (2014) In situ high-temperature experiments. Rev Mineral Geochem 78(1):779–800
Newcombe ME, Brett A, Beckett JR, Baker MB, Newman S, Guan Y, Stolper EM (2017) Solubility of water in lunar basalt at low pH2O. Geochim Cosmochim Acta 200:330–352
Ni P, Macris CA, Darling EA, Shahar A (2021) Evaporation-induced copper isotope fractionation: insights from laser levitation experiments. Geochim Cosmochim Acta 298:131–148
Nicholis MG, Rutherford MJ (2009) Graphite oxidation in the Apollo 17 orange glass magma: Implications for the generation of a lunar volcanic gas phase. Geochim Cosmochim Acta 73(19):5905–5917
Nishihara Y, Matsukage KN, Karato SI (2006) Effects of metal protection coils on thermocouple EMF in multi-anvil high-pressure experiments. Am Miner 91(1):111–114
Nordine PC, Atkins RM (1982) Aerodynamic levitation of laser-heated solids in gas jets. Rev Sci Instrum 53(9):1456–1464
O'Bannon EF, Jenei Z, Cynn H, Lipp MJ, Jeffries JR (2018) Contributed Review: Culet diameter and the achievable pressure of a diamond anvil cell: Implications for the upper pressure limit of a diamond anvil cell. Rev Sci Instrum 89(11):111501
O'Neill HSC (2005) A method for controlling alkali-metal oxide activities in one-atmosphere experiments and its application to measuring the relative activity coefficients of NaO0.5 in silicate melts. Am Mineral 90(2–3):497–501
Okuchi T (1997) Hydrogen partitioning into molten iron at high pressure: implications for Earth's core. Science 278(5344):1781–1784
Okuchi T, Takahashi E (1998) Hydrogen in molten iron at high pressure: the first measurement. Geophys Monogr Ser 101:249–260
Oran WA, Berge LH (1982) Containerless melting and solidification of materials with an aerodynamic levitation system. Rev Sci Instrum 53(6):851–853
Pack A, Kremer K, Albrecht N, Simon K, Kronz A (2010) Description of an aerodynamic levitation apparatus with applications in Earth sciences. Geochem Trans 11:1–16
Pan V, Holloway JR, Hervig RL (1991) The pressure and temperature dependence of carbon dioxide solubility in tholeiitic basalt melts. Geochim Cosmochim Acta 55(6):1587–1595
Pichavant M, Scaillet B, Pommier A, Iacono-Marziano G, Cioni R (2014) Nature and evolution of primitive Vesuvius magmas: an experimental study. J Petrol 55(11):2281–2310
Potapkin V, Chumakov AI, Smirnov GV, Celse JP, Rüffer R, McCammon C, Dubrovinsky L (2012) The 57Fe synchrotron Mössbauer source at the ESRF. J Synchrotron Radiat 19(4):559–569
Prabha-Mohan S, Koga KT, Mathieu A, Pointud F, Narvaez DF (2023) One-atmosphere high-temperature CO–CO_2–SO_2 gas-mixing furnace: design, operation, and applications. Eur J Mineral 35(3):321–331
Prescher C, Langenhorst F, Dubrovinsky LS, Prakapenka VB, Miyajima N (2014) The effect of Fe spin crossovers on its partitioning behavior and oxidation state in a pyrolitic Earth's lower mantle system. Earth Planet Sci Lett 399:86–91
Presnall DC, Brenner NL (1974) A method for studying iron silicate liquids under reducing conditions with negligible iron loss. Geochim Cosmochim Acta 38(12):1785–1788
Rai N, Van Westrenen W (2013) Core-mantle differentiation in Mars. J Geophys Res: Planets 118(6):1195–1203
Rai N, van Westrenen W (2014) Lunar core formation: new constraints from metal–silicate partitioning of siderophile elements. Earth Planet Sci Lett 388:343–352
Regier ME, Hervig RL, Myers ML, Roggensack K, Wilson CJ (2016) Analyzing nitrogen in natural and synthetic silicate glasses by secondary ion mass spectrometry. Chem Geol 447:27–39
Richter FM, Dauphas N, Teng FZ (2009) Non-traditional fractionation of non-traditional isotopes: evaporation, chemical diffusion and Soret diffusion. Chem Geol 258(1–2):92–103
Ripley EM, Li C, Moore CH, Elswick ER, Maynard JB, Paul RL, Shimizu N (2011) Analytical methods for sulfur determination in glasses, rocks, minerals and fluid inclusions. Rev Mineral Geochem 73(1):9–39

Rose-Weston L, Brenan JM, Fei Y, Secco RA, Frost DJ (2009) Effect of pressure, temperature, and oxygen fugacity on the metal-silicate partitioning of Te, Se, and S: implications for earth differentiation. Geochim Cosmochim Acta 73(15):4598–4615

Roskosz M, Bouhifd MA, Jephcoat AP, Marty B, Mysen BO (2013) Nitrogen solubility in molten metal and silicate at high pressure and temperature. Geochim Cosmochim Acta 121:15–28

Roskosz M, Amet Q, Fitoussi C, Dauphas N, Bourdon B, Tissandier L, Hu MY, Said A, Alatas A, Alp EE (2020) Redox and structural controls on tin isotopic fractionations among magmas. Geochim Cosmochim Acta 268:42–55

Rottier B, Audétat A (2019) In-situ quantification of chlorine and sulfur in glasses, minerals and melt inclusions by LA-ICP-MS. Chem Geol 504:1–13

Sarou-Kanian V, Rifflet JC, Millot F (2005) IR radiative properties of solid and liquid alumina: effects of temperature and gaseous environment. Int J Thermophys 26:1263–1275

Schanofski M, Koch L, Schmidt BC (2023) CO2 quantification in silicate glasses using μ-ATR FTIR spectroscopy. Am Miner 108(7):1346–1356

Schiavi F, Bolfan-Casanova N, Withers AC, Médard E, Laumonier M, Laporte D, Gómez-Ulla A (2018) Water quantification in silicate glasses by Raman spectroscopy: correcting for the effects of confocality, density and ferric iron. Chem Geol 483:312–331

Schilling F, Wunder B (2004) Temperature distribution in piston-cylinder assemblies: numerical simulations and laboratory experiments. Eur J Mineral 16(1):7–14

Shi L, Lu W, Kagoshima T, Sano Y, Gao Z, Du Z, Li Y (2022) Nitrogen isotope evidence for Earth's heterogeneous accretion of volatiles. Nat Commun 13(1):4769

Shilobreeva SN (2017) Secondary ion mass spectrometry in geochemistry and cosmochemistry: determination and distribution of carbon and hydrogen in silicate samples. J Anal Chem 72:1355–1368

Siebert J, Badro J, Antonangeli D, Ryerson FJ (2012) Metal–silicate partitioning of Ni and Co in a deep magma ocean. Earth Planet Sci Lett 321:189–197

Sinmyo R, Hirose K (2010) The Soret diffusion in laser-heated diamond-anvil cell. Phys Earth Planet Inter 180(3–4):172–178

Sossi PA, Klemme S, O'Neill HSC, Berndt J, Moynier F (2019) Evaporation of moderately volatile elements from silicate melts: experiments and theory. Geochim Cosmochim Acta 260:204–231

Sossi PA, Burnham AD, Badro J, Lanzirotti A, Newville M, O'Neill HSC (2020a) Redox state of Earth's magma ocean and its Venus-like early atmosphere. Sci Adv 6(48):1387

Sossi PA, Moynier F, Treilles R, Mokhtari M, Wang X, Siebert J (2020b) An experimentally-determined general formalism for evaporation and isotope fractionation of Cu and Zn from silicate melts between 1300 and 1500°C and 1 bar. Geochim Cosmochim Acta 288:316–340

Sossi PA, Tollan PM, Badro J, Bower DJ (2023) Solubility of water in peridotite liquids and the prevalence of steam atmospheres on rocky planets. Earth Planet Sci Lett 601:117894

Speelmanns IM, Schmidt MW, Liebske C (2018) Nitrogen solubility in core materials. Geophys Res Lett 45(15):7434–7443

Speelmanns IM, Schmidt MW, Liebske C (2019) The almost lithophile character of nitrogen during core formation. Earth Planet Sci Lett 510:186–197

Stanley BD, Hirschmann MM, Withers AC (2014) Solubility of COH volatiles in graphite-saturated martian basalts. Geochim Cosmochim Acta 129:54–76

Steven CJ, Dyar MD, McCanta M, Newville M, Lanzirotti A (2022) The absorption indicatrix as an empirical model to describe anisotropy in X-ray absorption spectra of pyroxenes. Am Mineral: J Earth Planet Mater 107(4):654–663

Suer TA, Siebert J, Remusat L, Menguy N, Fiquet G (2017) A sulfur-poor terrestrial core inferred from metal–silicate partitioning experiments. Earth Planet Sci Lett 469:84–97

Suer TA, Jackson C, Grewal DS, Dalou C, Lichtenberg T (2023) The distribution of volatile elements during rocky planet formation. Front Earth Sci 11:1159412

Sutton SR, Karner J, Papike J, Delaney JS, Shearer C, Newville M, Eng P, Rivers M, Dyar MD (2005) Vanadium K edge XANES of synthetic and natural basaltic glasses and application to microscale oxygen barometry. Geochim Cosmochim Acta 69:2333–2348

Tagawa S, Sakamoto N, Hirose K, Yokoo S, Hernlund J, Ohishi Y, Yurimoto H (2021) Experimental evidence for hydrogen incorporation into Earth's core. Nat Commun 12(1):2588

Taguchi S, Hasome H, Shimizu S, Ishiwata R, Inoue R, Yamada M, Watanabe M, Matsushita T, Ishikawa T, Oda H, Koyama C, Ito T (2023) Proposal of temperature correction of molten oxide based on its emissivity for measurement of temperature dependence of its density using ELF in ISS. Int J Microgravity Sci Appl 40(1):400101

Virgo D, Mysen BO (1985) The structural state of iron in oxidized vs. reduced glasses at 1 atm: A57Fe Mössbauer study. Phys Chem Minerals 12:65–76

von der Handt A, Dalou C (2016) Quantitative EPMA of nitrogen in silicate glasses. Microsc Microanal 22(S3):1810–1811

Wade J, Wood BJ (2005) Core formation and the oxidation state of the Earth. Earth Planet Sci Lett 236(1–2):78–95

Wagner C (1962) Thermodynamics of Alloys. Addison-Wesley, Reading

Walter MJ, Koga KT (2004) The effects of chromatic dispersion on temperature measurement in the laser-heated diamond anvil cell. Phys Earth Planet Inter 143:541–558

Wang YQ, Zhang J, Tesmer JR, Li YH, Greco R, Grim GP, Wilhelmy JB (2010) Determination of 13C/12C ratios with (d, p) nuclear reactions. Nucl Instrum Methods Phys Res Sect B: Beam Inter Mater Atoms 268(11–12):2099–2103

Waychunas GA, Fuller CC, Davis JA, Rehr JJ (2003) Surface complexation and precipitate geometry for aqueous Zn(II) sorption on ferrihydrite:II. XANES analysis and simulation. Geochim Cosmochim Acta 67:1031–1043

Wilke M, Behrens H (1999) The dependence of the partitioning of iron and europium between plagioclase and hydrous tonalitic melt on oxygen fugacity. Contrib Miner Petrol 137:102–114

Wilke M, Farges F, Petit PE, Brown GE Jr, Martin F (2001) Oxidation state and coordination of Fe in minerals: an Fe K-XANES spectroscopic study. Am Miner 86(5–6):714–730

Wilke M, Partzsch GM, Bernhardt R, Lattard D (2004) Determination of the iron oxidation state in basaltic glasses using XANES at the K-edge. Chem Geol 213:71–87

Wilke M, Klimm K, Kohn SC (2011) Spectroscopic studies on sulfur speciation in synthetic and natural glasses. Rev Mineral Geochem 73(1):41–78

Withers AC, Bureau H, Raepsaet C, Hirschmann MM (2012) Calibration of infrared spectroscopy by elastic recoil detection analysis of H in synthetic olivine. Chem Geol 334:92–98

Woodland AB, O'Neill HSC (1997) Thermodynamic data for Fe-bearing phases obtained using noble metal alloys as redox sensors. Geochim Cosmochim Acta 61(20):4359–4366

Yang L (2016) How to detect melting in laser heating diamond anvil cell. Chin Phys B 25(7):076201

Yang S, Zhaohui D (2011) Novel pressure-induced structural transformations of inorganic nanowires. In: Hashim A (ed) Nanowires—fundamental research. InTech, Rijeka

Yang X, Li Y (2016) High-P/T experimental studies and water in the silicate mantle. Sci China Earth Sci 59:683–695

Yaroslavtsev S, Chumakov AI (2022) Synchrotron Mössbauer source: trade-off between intensity and linewidth. J Synchrotron Rad 29:1329–1337

Yen CE, Williams Q, Kunz M (2020) Thermal pressure in the laser-heated diamond anvil cell: a quantitative study and implications for the density versus Mineralogy Correlation of the mantle. J Geophys Res: Solid Earth 125(10):20006

Yoshioka T (2018) Experimental studies on the deep geochemistry of carbon and nitrogen, Doctoral dissertation

Yoshioka T, Nakashima D, Nakamura T, Shcheka S, Keppler H (2019) Carbon solubility in silicate melts in equilibrium with a CO-CO_2 gas phase and graphite. Geochim Cosmochim Acta 259:129–143

Young ED, Macris CA, Tang H, Hogan AA, Shollenberger QR (2022) Isotope velocimetry: experimental and theoretical demonstration of the potential importance of gas flow for isotope fractionation during evaporation of protoplanetary material. Earth Planet Sci Lett 589:117575

Zajacz Z, Seo JH, Candela PA, Piccoli PM, Heinrich CA, Guillong M (2010) Alkali metals control the release of gold from volatile-rich magmas. Earth Planet Sci Lett 297:50–56

Zajacz Z, Seo JH, Candela PA, Piccoli PM, Tossell JA (2011) The solubility of copper in high-temperature magmatic vapors: a quest for the significance

of various chloride and sulfide complexes. Geochim Cosmochim Ac 75:2811–2827
Zajacz Z, Candela PA, Piccoli PM, Wälle M, Sanchez-Valle C (2012) Gold and copper in volatile saturated mafic to intermediate magmas: solubilities, partitioning, and implications for ore deposit formation. Geochim Cosmochim Acta 91:140–159
Zhai S, Ito E (2011) Recent advances of high-pressure generation in a multi-anvil apparatus using sintered diamond anvils. Geosci Front 2(1):101–106
Zhang HL, Hirschmann MM, Cottrell E, Newville M, Lanzirotti A (2016) Structural environment of iron and accurate determination of Fe^{3+}/ΣFe ratios in andesitic glasses by XANES and Mössbauer spectroscopy. Chem Geol 428:48–58
Zhang HL, Hirschmann MM, Cottrell E, Withers AC (2017) Effect of pressure on Fe^{3+}/ΣFe ratio in a mafic magma and consequences for magma ocean redox gradients. Geochim Cosmochim Acta 204:83–103
Zube NG, Nimmo F, Fischer RA, Jacobson SA (2019) Constraints on terrestrial planet formation timescales and equilibration processes in the Grand Tack scenario from Hf-W isotopic evolution. Earth Planet Sci Lett 522:210–218

Publisher's Note

Springer Nature remains neutral with regard to jurisdictional claims in published maps and institutional affiliations.